Mechanical Systems and Signal Processing 248 (2026) 114013

Contents lists available at ScienceDirect

Mechanical Systems and Signal Processing

journal homepage: www.elsevier.com/locate/ymssp

Full length article

Physics-informed neural operators for predicting structural intensity from laser Doppler vibrometry measurements of plates

Johannes D. Schmid [a],[*], Sebastian F. Zettel [a,b], Steffen Marburg [a]

[a] Technical University of Munich, School of Engineering and Design, Chair of Vibroacoustics of Vehicles and Machines, Boltzmannstr. 15, 85748, Garching near Munich, Germany
[b] German Aerospace Center (DLR), Institute of Aeroelasticity, Bunsenstr. 10, 37073, Göttingen, Germany

ARTICLE INFO

Communicated by E. Chatzi

Keywords:
Structural intensity
Operator learning
Neural operators
Machine learning
Neural networks
DeepONets
PINNs

ABSTRACT

Structural intensity is a powerful diagnostic tool for characterizing vibrational energy flow and identifying dominant transfer paths in structures. For thin-walled plates, the structural intensity can be computed from the transverse displacement field and its spatial derivatives. However, accurate estimation from experimental data remains challenging, as numerical differentiation is highly sensitive to measurement noise, particularly when computing higher-order spatial gradients. This study proposes a machine learning-based framework employing a physics-informed deep operator network to predict structural intensity directly from noisy displacement measurements. Instead of differentiating raw measurement data, the method first learns a smooth, fully differentiable neural-network surrogate of the displacement field, enabling stable and accurate evaluation of higher-order spatial derivatives via automatic differentiation. This eliminates noise-induced instabilities of conventional numerical differentiation methods and enables robust structural intensity prediction from experimental data. The methodology is assessed using two case studies: an analytical benchmark problem of a simply supported plate, and experimental laser Doppler vibrometry measurements of a plate structure for practical validation. The results demonstrate that the physics-informed deep operator network accurately predicts the displacement and structural intensity fields over a broad frequency range, capturing both magnitude distributions and directional patterns with high fidelity. Across all studies, the proposed data-driven approach consistently outperforms numerical differentiation techniques, demonstrating enhanced robustness and accuracy while confirming its applicability to problems in experimental structural dynamics and noise control engineering.

1. Introduction

The identification of dominant structural energy transfer paths and the assessment of vibrational energy flow within a structure are essential diagnostic tools in noise and vibration control. By localizing these dominant transfer paths, targeted countermeasures can be implemented to attenuate the propagated energy before it reaches regions of efficient airborne sound radiation. As Pavić [1] has emphasized, vibroacoustic isolation of the vibrating source alone is often not sufficient for an effective reduction of sound radiation. Instead, it is generally more effective to attenuate the mechanical energy transported by structural waves along the propagation paths, thereby preventing the energy from reaching regions that are efficient radiators of airborne sound. This issue is particularly critical for flexural waves in thin-walled, plate-like structures commonly found in engineering applications.

---

[*] Corresponding author.
E-mail address: johannes.d.schmid@tum.de (J.D. Schmid).

https://doi.org/10.1016/j.ymssp.2026.114013
Received 18 August 2025; Received in revised form 9 February 2026; Accepted 10 February 2026

These structures are typically lightly damped and easily excited, making them efficient radiators of structure-borne sound [1]. Consequently, mitigating energy transmission within the structure plays a key role in reducing sound radiation of structure-borne sound as the source of secondary airborne sound.

While established techniques such as transfer path analysis [2] are widely used for characterizing structural vibrations, they primarily characterize the dynamic response of a system and the ratio of vibration levels between source and receiver points. However, these methods do not provide spatially resolved information about the actual transmission paths of vibrational energy. To address this limitation, the concept of structural intensity (STI) has been introduced [3]. Defined as the rate of mechanical energy flow per unit area, STI allows for a spatially resolved and direction-dependent assessment of vibrational energy propagation. This enables the identification of energy transmission paths, source and sink regions, and local dissipation phenomena. The analysis of STI offers a deeper understanding of the dynamic behavior of structures, particularly when conventional vibration metrics fall short in describing complex energy pathways.

1.1. *Measurement techniques for structural intensity*

The concept of STI has first been introduced by Noiseux [3] in 1970, who has proposed a method for measuring vibrational power flow in uniform beams and plates using biaxial accelerometers. This seminal approach has enabled simultaneous measurement of translational and rotational velocity components, facilitating the estimation of energy flux associated with elastic wave propagation. Building upon this framework, Pavić [1] has introduced the use of finite difference approximations to compute spatial derivatives from measured velocity fields. This development has enabled the estimation of power flow induced by flexural waves in beams and plates, using sensor arrays configured in 4-point and 8-point layouts in combination with digital signal processing techniques. Verheij [4] has advanced STI measurement methodology by introducing cross-spectral density methods, while Fahy and Pierri [5] further refined these methods to address phase mismatch issues across measurement channels.

Early STI studies have primarily relied on the finite difference method to approximate spatial derivatives [1]. As an alternative, Williams et al. [6] have proposed a wavenumber-domain approach based on spatial Fourier transforms. This class of methods, later referred to as k-space methods by Morikawa et al. [7], have demonstrated enhanced robustness under noisy measurement conditions [8,9].

Despite the significant insights provided by these early contributions, they share a fundamental limitation: They all rely on contact-based measurement techniques. Typically, such approaches use accelerometers in conjunction with finite difference schemes to approximate spatial gradients. A fundamental drawback of contact-based structural intensity measurement techniques is the sensor-induced mass loading effect, where the added mass of the transducers alters the dynamic behavior of the structure under investigation. This mass-induced modification can significantly distort the measured response, which becomes particularly problematic in thin-walled and lightweight structures. Beyond mass loading, these methods are prone to various other sources of uncertainties, including transducer misalignment, phase mismatch between transducer channels, limited spatial resolution, and discretization errors from finite difference approximations, where dense sensor placement may not be feasible.

To overcome these limitations of contact-based methods, the field transitioned towards non-contact and optical measurement techniques. Laser Doppler vibrometry (LDV) [10,11] has emerged as the most widely adopted technology, providing high spatial resolution without introducing mass loading effects [12,13]. Weisbecker et al. [14] have used scanning LDV for non-contact measurement of dynamic surface strain fields across planar structures subject to in-plane loading. Pascal et al. [15] have used scanning LDV to assess STI and energy dissipation across joints in plate assemblies. Other optical measurement techniques include holographic interferometry [16], near-field acoustic holography [17], electronic speckle pattern interferometry [18], and digital stroboscopic holography [19], all of which provide full-field, high-resolution measurements of surface velocity fields. In more recent developments, stereo camera systems have been employed to achieve dense, full-field 3D displacement measurements without the need for pointwise scanning [20]. Egner et al. [21] applied a stereo camera system combined with polynomial filtering to compute STI fields on curved plates. Recently, Meteyer et al. [22] apply optical deflectometry, a single-camera technique that estimates surface slopes from reflected grid patterns, to capture time- and space-resolved STI fields.

1.2. *Numerical estimation of structural intensity*

In addition to experimental techniques, the increasing availability of computational resources has facilitated STI analysis through numerical simulation. Among numerical approaches, the finite element method (FEM) has played a central role in advancing modern STI analysis. In FEM-based STI formulations, the required spatial derivatives are obtained directly from the interpolation functions of the finite elements, providing a mathematically rigorous and geometrically flexible approach of evaluating STI in complex structures. One of the earliest finite element implementations of STI has been introduced by Hambric [23], who demonstrated its applicability on beam-stiffened cantilever plates and truss structures. Gavrić and Pavić [24] have later applied the normal mode approach within the FEM framework to evaluate STI in simply supported plates, which was later extended to experimental data by Gavrić et al. [25]. Since then, FEM-based STI formulations have been extended to include a broad range of structural elements, including solid elements [26], beam elements [27], flat plate structures [28,29], and curved shell elements [20,30]. These developments have firmly established the FEM as a robust and widely adopted tool for STI analysis in both research and engineering application.

1.3. Applications of structural intensity

Since then, STI has emerged as a powerful diagnostic tool across a wide range of engineering applications and it has been widely applied across various fields and structural systems. In the field of composite structures, STI has been applied to numerical modeling [31] and to investigate the influence of geometric discontinuities and material anisotropy. Xu et al. [32] analyze energy propagation in composite plates with cut-outs, while Petrone et al. [33] conduct parametric studies on orthotropic plates, examining the effects of boundary conditions, damping, and fiber orientation. In the context of passive vibration control, Khun et al. [28] employ STI to evaluate the effectiveness of local damping treatments, such as discrete or distributed dampers, and to guide the placement of dissipative elements for optimal energy attenuation. Xu et al. [34] employ STI to analyze the energy flow in stiffened plates of marine structures, while Schaal et al. [35] establish a relation between the STI fields and sound radiation of plate-rib models. In the field of structural health monitoring, STI maps have been used to detect and localize structural damages by identifying anomalies in energy flow [36]. Although early STI applications focused primarily on flat plates and beam-like structures, recent developments have extended its use to curved shell structures through curvilinear coordinate formulations [20,21,37], which requires full-field 3D measurements due to the significance of in-plane vibrational components. Recent advances expand the use of STI to periodic and locally resonant elastic metamaterials [38] to investigate bandgap formation and energy attenuation mechanisms. Most recently, STI has been employed to analyze energy concentration and damping mechanisms in acoustic black hole structures, offering new insights into passive vibration control [39,40].

1.4. Machine learning methods in structural dynamics

Over the past decades, machine learning has emerged as a powerful paradigm in scientific computing, offering new capabilities for modeling and solving complex physical systems [41]. Unlike traditional numerical methods such as the FEM [42], which require mesh generation and often become computationally expensive for parameterized and high-dimensional problems, machine learning methods are inherently mesh-free, enable evaluations at arbitrary spatial resolutions, and offer superior scalability in high-dimensional problems [43]. A key advancement in this field is the development of physics-informed machine learning, where prior knowledge about the governing physical laws, is embedded into the training process. Physics-informed neural networks (PINNs), introduced by Raissi et al. [44], incorporate the residuals of partial differential equations (PDEs) and associated boundary conditions into the loss function of a neural network. This approach ensures that the learned solutions are consistent with underlying physical principles, thereby enhancing robustness and generalization capabilities even in the presence of noisy or incomplete training data [45]. PINNs have been successfully applied across a broad range of applications, including fluid dynamics [46], acoustics [47,48], and elastodynamics [49,50]. In the field of structural dynamics, applications of PINNs include analysis of plates [51,52], shell structures [53], dynamic stress field estimation [54], modeling of moving load conditions [55], as well as inverse problems like damage detection [56,57].

Despite their advantages, both FEM and PINNs are inherently limited to solving PDEs for a fixed set of input parameters. A fundamental limitation of both FEM and PINNs lies in their restriction to single-instance solutions, meaning that they typically solve the PDE for one fixed set of PDE input parameters. As a result, any change in input parameters, such as frequency, boundary conditions, or load cases, requires retraining or recomputation. This makes them inefficient for parameterized problems, such as frequency-dependent simulations in structural dynamics, where solutions must be computed across a broad range of input conditions.

To address this limitation, the concept of operator learning has recently emerged [58]. Rather than solving PDEs pointwise for individual input parameter sets, neural operators aim to approximate the entire solution operator that maps input functions (such as coefficients, frequencies, or excitations) to output functions (the solution field of interest) [59,60]. Once trained, the neural operator enables efficient and accurate predictions of the solution field for any new instance of the input function (e.g. new frequency step) with negligible computational cost, making them highly suitable for parameterized simulations and real-time applications.

A seminal contribution in this field is the deep operator network (DeepONet) introduced by Lu et al. [61], which provides a framework for approximating nonlinear continuous operators with minimal generalization error. Building upon this work, several neural operator architectures have been proposed, including Fourier neural operators [62] and graph neural operators [63]. In the context of structural mechanics, neural operators have demonstrated strong performance in diverse applications. These include the prediction of stress fields in elastoplastic structures [64,65], the learning of stress–strain relationships in composites [66], and the solution of inverse problems for parameter identification [67]. Moreover, they have been employed for the design and characterization of mechanical [68] and acoustical metamaterials [69], as fast surrogates in shape optimization workflows [70], for crack prediction in brittle fracture mechanics [71], and for the simulation of sound propagation in virtual environments with parameterized source positions [72]. These developments underscore the potential of neural operators to bridge the gap between data-driven learning and physics-based modeling, enabling fast, accurate, and generalizable solutions for complex, parameterized systems.

1.5. Main contributions

Despite substantial advances in STI research, accurately estimating STI fields from experimental data remains a critical challenge. A key limitation lies in the need to compute high-order spatial derivatives from the measured displacement field, specifically third-order derivatives, which are required to derive the STI field from displacement data. In practice, measurement data are inherently corrupted by noise, or discretization artifacts. Numerical differentiation of these measurement signals is highly sensitive to noise and prone to amplification of errors, which can significantly degrade the accuracy of the resulting STI prediction. Although various smoothing [73] and filtering [74] techniques have been proposed to mitigate these issues, the fundamental limitations of numerical differentiation in the presence of noisy data remain unresolved.

This work proposes a novel, machine learning-based framework for the estimation of structural intensity, leveraging the recent advances in physics-informed neural networks and operator learning. Specifically, a methodology based on physics-informed DeepONets is presented for predicting the STI fields directly from noisy displacement measurements. In contrast to traditional methods relying on numerical differentiation, the proposed approach learns a smooth, fully differentiable surrogate model from displacement measurements, enabling direct and stable evaluation of high-order spatial derivatives via automatic differentiation. This bypasses the instabilities typically associated with noise-amplifying numerical gradient computations and ensures an accurate estimation of the STI, even in the presence of noisy measurement data. Furthermore, the methodology integrates physical knowledge by incorporating the residual of the Kirchhoff–Love plate equation into the training loss, thereby ensuring physical consistency of the learned solution and enhancing generalization across spatial and parametric variations. This methodology advances the state of the art in STI analysis and highlights the potential of operator learning in experimental structural dynamics and noise control engineering.

The structure of this article is as follows: Section 2 provides the theoretical background on structural intensity in plate structures. Section 3 introduces the concept of neural operators, with a particular focus on physics-informed DeepONets incorporating the Kirchhoff–Love plate equation. In Section 4, an analytical plate example is presented to demonstrate the methodology and examine the influences of parameter variations. Section 5 describes the LDV measurement setup and provides experimental validation of the STI predictions derived from measurement data. Section 6 concludes the paper by summarizing the key findings and outlining perspectives for future research.

2. Structural intensity in plates

Structural intensity is defined as the vibrational power flow per unit cross-sectional area transmitted by elastic waves within a solid medium. In analogy to acoustic intensity in fluids, it provides a directional measure that describes the flow of mechanical energy associated with vibrational energy propagation. It facilitates the identification of dominant transmission paths, energy sources and sinks, and regions of localized dissipation. In a general elastic solid, the complex-valued structural intensity vector field in the frequency domain, denoted by $\mathbf{I}(\mathbf{x},\omega)$ at position $\mathbf{x}$, is defined as the product of the stress tensor $\boldsymbol{\sigma}(\mathbf{x},\omega)$ and the complex conjugate of the velocity vector $\mathbf{v}^*(\mathbf{x},\omega)$, as

$$\mathbf{I}(\mathbf{x},\omega) = -\frac{1}{2}\boldsymbol{\sigma}(\mathbf{x},\omega)\cdot\mathbf{v}^*(\mathbf{x},\omega), \qquad \mathbf{x}\in\Omega. \tag{1}$$

In this formulation, all field quantities are represented as complex-valued amplitudes, ω denotes the angular frequency, Ω is the computational domain, and * indicates the complex conjugate. The negative sign in the definition arises from the sign convention for stress directions, as discussed by Pavić [75]. The complex-valued structural intensity vector can be decomposed into two physically meaningful components. The active intensity, given by the real part $\Re\{\mathbf{I}\}$, which quantifies the net energy flow through the structure. And the reactive intensity, corresponding to the imaginary part $\Im\{\mathbf{I}\}$, which represents oscillatory, non-propagating energy exchange that does not contribute to net energy flow. While this general formulation is valid for arbitrary three-dimensional elastic solids, many engineering applications are concerned with thin-walled structures, as flexural waves dominate their vibrational energy transport [16] and these structures are key contributors to structure-borne sound radiation.

This work focuses on isotropic, thin-walled plates subjected to purely transverse, time-harmonic excitation in the frequency domain. The analysis of STI in plate structures is commonly based on the Kirchhoff–Love plate theory, which simplifies the kinematic relationships by assuming that normals to the mid-surface remain straight and normal after deformation and do not experience transverse shear deformation [76]. Under these assumptions, the full three-dimensional displacement field can be expressed entirely in terms of the out-of-plane transverse displacements $w(\mathbf{x})$ and its spatial derivatives, where $\mathbf{x} = [x, y]$. For the sake of brevity, in the subsequent derivation, the notation $w(\mathbf{x}) = w$ is used. In particular, the in-plane displacements are governed by the bending rotations, which can directly be obtained as the spatial gradients of w, as

$$\varphi_x = \frac{\partial w}{\partial y}, \quad \varphi_y = -\frac{\partial w}{\partial x}. \tag{2}$$

Under the assumptions of Kirchhoff–Love plate theory, the governing equation for the transverse motion of a linear, isotropic, and homogeneous plate subjected to time-harmonic transverse loading in the frequency domain is given by the fourth-order partial differential equation

$$D\left(\frac{\partial^4 w}{\partial x^4} + 2\frac{\partial^4 w}{\partial x^2 \partial y^2} + \frac{\partial^4 w}{\partial y^4}\right) - \omega^2 \rho h\, w = \psi(\mathbf{x}), \tag{3}$$

where w denotes the complex-valued amplitude of the transverse displacement, and $\psi(\mathbf{x})$ represents the externally applied transverse load per unit area. The parameter $D = \frac{Eh^3}{12(1-\mu^2)}$ defines the flexural rigidity of the plate, where E is Young's modulus, μ is Poisson's ratio, h is the plate thickness, and ρ is the mass density of the material. In purely flexural wave fields, vibrational energy is primarily transported by bending and twisting moments, as well as transverse shear forces.

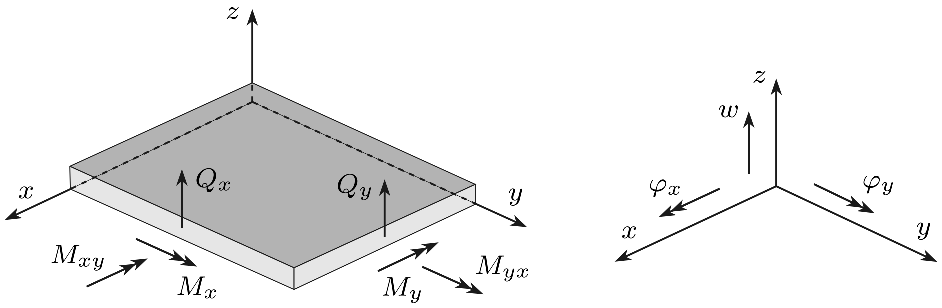

Fig. 1. Schematic sketch of a Kirchhoff–Love plate element in the x-y plane, showing all internal section forces and moments, as well as the deformations and rotations. It includes bending moments M_x, M_y, twisting moment M_{xy}, M_{yx}, shear forces Q_x, Q_y, bending rotations φ_x, φ_y, and the transverse displacement w.

Fig. 1 shows the section forces and moments, as well as the displacements and rotations of a plate with the mid-surface lying in the xy-plane. The bending moments M_x, M_y and twisting moment M_{xy}, M_{yx} per unit width in an isotropic Kirchhoff–Love plate are expressed in terms of the transverse displacement field w, as

$$\begin{aligned} M_x &= -D\left(\frac{\partial^2 w}{\partial x^2} + \mu \frac{\partial^2 w}{\partial y^2}\right), \\ M_y &= -D\left(\frac{\partial^2 w}{\partial y^2} + \mu \frac{\partial^2 w}{\partial x^2}\right), \\ M_{xy} &= -D(1-\mu)\frac{\partial^2 w}{\partial x \partial y}, \end{aligned} \tag{4}$$

where $M_{yx} = M_{xy}$ due to symmetry. The associated transverse shear forces Q_x, Q_y per unit width are given by

$$\begin{aligned} Q_x &= -D\frac{\partial}{\partial x}\left(\frac{\partial^2 w}{\partial x^2} + \frac{\partial^2 w}{\partial y^2}\right) = -D\frac{\partial}{\partial x}\left(\nabla^2 w\right), \\ Q_y &= -D\frac{\partial}{\partial y}\left(\frac{\partial^2 w}{\partial x^2} + \frac{\partial^2 w}{\partial y^2}\right) = -D\frac{\partial}{\partial y}\left(\nabla^2 w\right), \end{aligned} \tag{5}$$

where ∇^2 denotes the Laplace operator. For a flat plate, the STI vector reduces to a two-dimensional vector lying in the mid-surface of the plate and is defined by the time-averaged vibrational power flow per unit width. Based on section forces and internal moments, the active STI vector $\mathbf{I} = [I_x, I_y]$ in the frequency domain is given by

$$\begin{aligned} I_x &= -\frac{\omega}{2}\Im\left\{Q_x w^* + M_x \varphi_y^* - M_{xy}\varphi_x^*\right\}, \\ I_y &= -\frac{\omega}{2}\Im\left\{Q_y w^* - M_y \varphi_x^* + M_{yx}\varphi_y^*\right\}. \end{aligned} \tag{6}$$

In this formulation, the first term in each component accounts for power flow due to shear forces, while the remaining terms represent contributions from bending and twisting moments. Although this formulation based on section forces and moments is well-suited for STI calculation based on the FEM, it is very difficult to measure the internal forces and moments simultaneously at the same position. For this reason, a purely displacement-based formulation is often preferred for measurement-based STI analysis [77]. By substituting Eqs. (2) and (4)–(5) into Eq. (6), the active STI components can be reformulated in terms of the transverse displacement w only, as

$$\begin{aligned} I_x &= -\frac{\omega}{2} D\,\Im\left\{-\frac{\partial}{\partial x}\left(\frac{\partial^2 w}{\partial x^2} + \frac{\partial^2 w}{\partial y^2}\right) w^* + \left(\frac{\partial^2 w}{\partial x^2} + \mu\frac{\partial^2 w}{\partial y^2}\right)\left(\frac{\partial w^*}{\partial x}\right) + (1-\mu)\frac{\partial^2 w}{\partial x \partial y}\left(\frac{\partial w^*}{\partial y}\right)\right\}, \\ I_y &= -\frac{\omega}{2} D\,\Im\left\{-\frac{\partial}{\partial y}\left(\frac{\partial^2 w}{\partial x^2} + \frac{\partial^2 w}{\partial y^2}\right) w^* + \left(\frac{\partial^2 w}{\partial y^2} + \mu\frac{\partial^2 w}{\partial x^2}\right)\left(\frac{\partial w^*}{\partial y}\right) + (1-\mu)\frac{\partial^2 w}{\partial x \partial y}\left(\frac{\partial w^*}{\partial x}\right)\right\}. \end{aligned} \tag{7}$$

Finally, the magnitude of the active STI vector is given by

$$|\mathbf{I}| = \sqrt{I_x^2 + I_y^2}. \tag{8}$$

Fig. 2 provides a schematic overview of the process for deriving STI from the transverse displacement field w. It illustrates the hierarchical relationship between the intermediate quantities, and systematically classifies them according to their respective order of spatial derivative. From the figure, it becomes clear that the calculation of STI requires the evaluation of spatial derivatives of the transverse displacement field up to third order.

It is worth emphasizing that when employing displacement-based formulations rather than velocity-based ones under the time-harmonic assumption of $e^{\mathrm{i}\omega t}$, the expression for time-averaged active STI involves the imaginary part of the product of force and

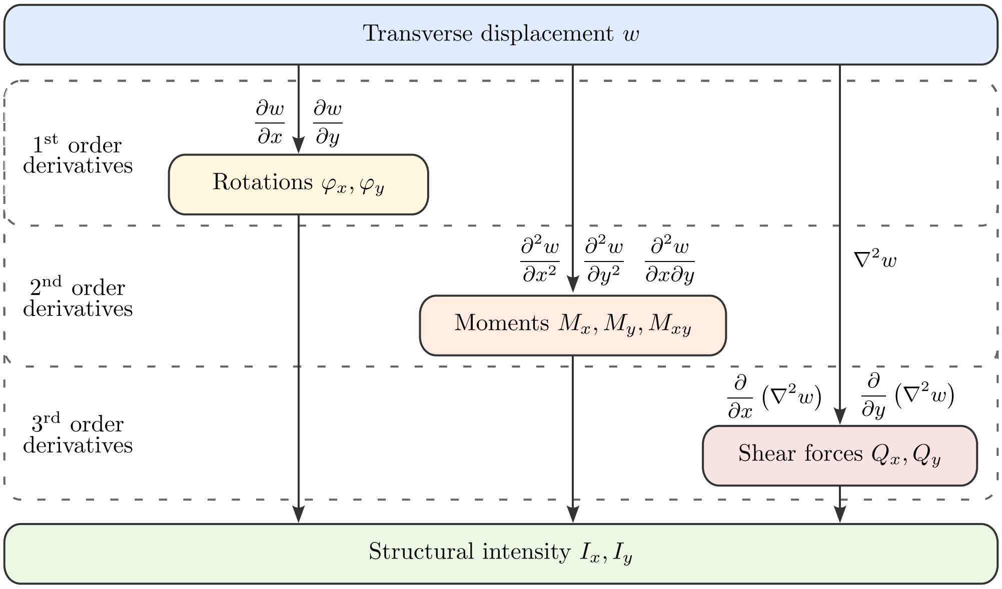

Fig. 2. Illustration of the process for deriving STI (I_x, I_y) from the transverse displacement field w. The required quantities, namely rotations (φ_x, φ_y), moments (M_x, M_y, M_{xy}), and shear forces (Q_x, Q_y) are categorized according to their respective orders of derivatives.

displacement. This results from the fact that, in the frequency domain, temporal differentiation introduces a multiplicative factor of $\mathrm{i}\omega$, thereby shifting the real part of the force–velocity product into the imaginary part of the force–displacement product. It should also be noted that the STI in this formulation is expressed as power per unit width, with units of $\mathrm{W\,m^{-1}}$.

3. Physics-informed neural operators

It is well established that neural networks serve as universal function approximators, capable of approximating any continuous function to arbitrary accuracy using a single hidden layer with a sufficient number of neurons [78]. Extending this concept to functional mappings, Chen and Chen [79] have proven the universal approximation theorem for nonlinear operators. This theorem states that a neural network with a single hidden layer is able to approximate any continuous nonlinear operator with arbitrary accuracy, provided the network width is sufficiently large. This insight laid the theoretical foundation for the emerging field of operator learning. Neural operators can be interpreted as a generalization of neural networks, designed to learn mappings between infinite-dimensional function spaces.

Neural operators offer several methodological advantages. First, they provide amortized inference, meaning that once trained, they can be evaluated for new input functions without retraining, thereby generalizing to previously unseen configurations. Second, they are inherently mesh-free and can be evaluated at arbitrary spatial resolutions and grid configurations. Third, neural operators, by construction, disentangle spatial structure from parametric dependence. This feature separation stabilizes training by enabling the model to learn spatial patterns and parametric dependencies independently, which better captures nonlinear cross-dependencies. Finally, neural operators are continuously differentiable with respect to their inputs and support automatic differentiation, facilitating derivative-based post-processing such as sensitivity analysis or the computation of physical quantities like the STI.

3.1. *Fundamentals of neural operators*

In this work, the nonlinear solution operator $\mathcal{G}$ associated with the frequency-parameterized Kirchhoff–Love plate equation, cf. Eq. (3), which maps a frequency input function f to the corresponding transverse displacement field $w(\mathbf{x})$, is considered as

$$\mathcal{G} : f \mapsto w(\mathbf{x}), \quad \mathbf{x} \in \Omega. \tag{9}$$

Here, the solution operator $\mathcal{G}$ maps between the infinite-dimensional function spaces of admissible input and output functions $\mathcal{G} : \mathcal{F} \to \mathcal{W}$, where the output can be evaluated, as

$$w(f)(\mathbf{x}) = \mathcal{G}(f)(\mathbf{x}), \quad w \in \mathcal{W}, \quad f \in \mathcal{F}. \tag{10}$$

The objective of operator learning is to approximate the operator $\mathcal{G}$ by a neural network-based surrogate model $\mathcal{G}_\theta : \mathcal{F} \to \mathcal{W}$, parameterized by the trainable weights and biases of the neural network, such that

$$\mathcal{G}_\theta(f)(\mathbf{x}) = w_\theta(f)(\mathbf{x}) \approx \mathcal{G}(f)(\mathbf{x}), \quad \forall f \in \mathcal{F}, \quad \mathbf{x} \in \Omega, \tag{11}$$

where $w_\theta(f)(\mathbf{x})$ denotes the neural operator prediction of the transverse displacement field. The trainable neural network parameters θ are obtained by minimizing a suitable loss functional $\mathcal{L}$ that quantifies the discrepancy between the predicted and reference solutions over the training data set, resulting in the minimization problem

$$\theta^* = \arg\min_\theta \mathcal{L}\Big(\mathcal{G}_\theta(f)(\mathbf{x}), \mathcal{G}(f)(\mathbf{x})\Big), \tag{12}$$

where θ^* is the optimized set of neural network parameters after the training has converged. Once trained, the neural operator $\mathcal{G}_\theta$ enables fast and mesh-independent predictions for any new frequency $\hat{f} \in \mathcal{F}$ to predict the corresponding displacement field $\hat{w}(\mathbf{x}) = \mathcal{G}_\theta(\hat{f})(\mathbf{x})$ in a single forward pass of the pre-trained neural operator without requiring retraining. This makes neural operators particularly interesting for parameterized problems, where solutions are required across a broad range of input conditions without the need for repeated retraining.

3.2. Deep operator networks (DeepONets)

The DeepONet architecture, introduced by Lu et al. [61], represents the first practical implementation of a neural operator. Inspired by the universal approximation theorem for operators [79], DeepONets have emerged as an effective framework for learning mappings between function spaces, due to its theoretical foundation and strong empirical performance in a wide range of physical problems [80,81].

The core concept of DeepONets is to decompose the operator learning task into two sub-networks: one that encodes the input function f and another one that evaluates the output at specific locations $\mathbf{x}$. Specifically, the DeepONet architecture consists of a branch network and a trunk network. The branch network processes the discretized input frequency function $f^{(i)} = [f^{(1)}, f^{(2)}, \dots, f^{(N_\mathrm{f})}]^T \in \mathbb{R}^{N_\mathrm{f}}$, and outputs a feature vector $b_k = [b_1, b_2, \dots, b_p]^T \in \mathbb{R}^p$. The trunk network takes a spatial evaluation point $\mathbf{x} \in \Omega \subset \mathbb{R}^r$ and returns another feature vector $t_k = [t_1, t_2, \dots, t_p]^T \in \mathbb{R}^p$. The operator output at frequency f and location $\mathbf{x}$ is obtained as the dot product of the two branch and trunk feature vectors, as

$$\mathcal{G}_\theta(f)(\mathbf{x}) = \sum_{k=1}^{p} \underbrace{b_k\left(f^{(1)}, f^{(2)}, \dots, f^{(N_\mathrm{f})}\right)}_{\text{branch}} \cdot \underbrace{t_k(\mathbf{x})}_{\text{trunk}}, \tag{13}$$

where θ denotes all trainable weights and biases of the branch and trunk networks.

This formulation can be interpreted in analogy to the classical modal superposition, where the trunk network learns a set of spatial basis functions (mode shapes) $t_k(\mathbf{x})$, while the branch network determines the frequency-dependent coefficients (modal participation factors) $b_k(f)$ [82,83]. By explicitly decoupling spatial and parametric (frequency) dependencies, the DeepONet architecture leverages the underlying modal structure and decomposes the learning task into two simpler subtasks. The trunk network learns a reusable set of frequency-independent spatial patterns $t_k(\mathbf{x})$, and the branch network learns how their coefficients $b_k(f)$ evolve with frequency.

This disentanglement is particularly beneficial near resonance frequencies, where the amplitude of $w(\mathbf{x})$ varies sharply with frequency while the spatial patterns remain well represented by the same bases $t_k(\mathbf{x})$. A frequency-parameterized PINN instead learns an entangled mapping $(\mathbf{x}, f) \to w_\theta(\mathbf{x}, f)$ using a single neural network, which is typically less stable and less accurate than the DeepONet structure.

The model is trained on a training dataset of labeled triplets, each consisting of an input frequency function $f^{(i)}$, a spatial evaluation point $\mathbf{x}_\mathrm{tr}^{(i,j)}$, and a corresponding reference displacement value $\bar{w}(f^{(i)})(\mathbf{x}_\mathrm{tr}^{(i,j)})$. The training dataset is formally expressed as

$$\mathcal{D}_\mathrm{tr} = \left\{ \left(f^{(i)}, \mathbf{x}_\mathrm{tr}^{(i,j)}, \bar{w}\big(f^{(i)}\big)\big(\mathbf{x}_\mathrm{tr}^{(i,j)}\big) \right) \middle| \; i = 1, \dots, N_\mathrm{f};\; j = 1, \dots, N_\mathrm{tr} \right\}, \tag{14}$$

where $f^{(i)} \in \mathcal{F}$ denotes the ith frequency input function, $\mathbf{x}_\mathrm{tr}^{(i,j)} \in \Omega$ is the jth spatial training data point associated with $f^{(i)}$, and $\bar{w}\big(f^{(i)}\big)\big(\mathbf{x}_\mathrm{tr}^{(i,j)}\big) \in \mathbb{C}$ represents the corresponding true transverse displacement solution evaluated at the associated training data point j and frequency i. N_f denotes the total number of frequency samples, and N_tr represent the total number of training points per frequency. It should be noted that in the scope of this work, the frequency input function is a constant function.

For purely supervised learning, the model is optimized by minimizing the mean squared error (MSE) [61] between the predicted neural operator outputs w_θ and the true displacement values $\bar{w}$, across all training samples. The resulting data-driven MSE loss function is given by

$$\mathcal{L}_\mathrm{data}(\theta) = \frac{1}{N_\mathrm{f}} \frac{1}{N_\mathrm{tr}} \sum_{i=1}^{N_\mathrm{f}} \sum_{j=1}^{N_\mathrm{tr}} \left| w_\theta\big(f^{(i)}\big)\big(\mathbf{x}_\mathrm{tr}^{(i,j)}\big) - \bar{w}\big(f^{(i)}\big)\big(\mathbf{x}_\mathrm{tr}^{(i,j)}\big) \right|^2. \tag{15}$$

This formulation enables the DeepONet to generalize across variations in the frequency space $f \in \mathcal{F}$ as well as arbitrary evaluation points in the spatial domain $\mathbf{x} \in \Omega$, facilitating flexible and efficient operator inference under a wide range of parametric input conditions.

3.3. Kirchhoff–Love-plate-theory-informed neural operators

Physics-informed DeepONets, introduced by Wang et al. [84], extend the DeepONet framework by incorporating the governing physical laws directly into the training process. This is achieved by embedding the residuals of the underlying PDE into the loss function, such that the model simultaneously learns from data and respects the physical constraints. By minimizing the loss function during training, the model learns a solution that not only fits the data but also satisfies the underlying physical principles, thereby improving generalization and physical consistency.

In the present work, the Kirchhoff–Love plate equation in the frequency-domain, as introduced in Section 2 and defined in Eq. (3), serves as the governing PDE. Due to its fourth-order nature, direct enforcement of the PDE residual often results in numerical instabilities during training, especially due to exploding gradients when computing high-order derivatives. To mitigate this, the PDE is reformulated using an auxiliary variable, which decomposes the original fourth-order PDE into a system of two second-order equations, as

$$\begin{aligned} q(\mathbf{x}) &= \nabla^2 w(\mathbf{x}), \\ \nabla^2 q(\mathbf{x}) - \frac{\omega^2 \rho h}{D} w(\mathbf{x}) &= 0, \end{aligned} \tag{16}$$

where $q(\mathbf{x})$ denotes the Laplacian of the transverse displacement $w(\mathbf{x})$. This reformulation in two second-order equations avoids direct computation of fourth-order derivatives, significantly improving numerical stability during training.

The physics-based loss $\mathcal{L}_{\mathrm{phys}}$, evaluated for the DeepONet predictions w_θ and q_θ, then consists of two loss components: the auxiliary loss $\mathcal{L}_{\mathrm{aux}}$, which enforces the identity constraint $q_\theta = \nabla^2 w_\theta$, and the PDE-loss $\mathcal{L}_{\mathrm{PDE}}$, which enforces the fulfillment of the reformulated Kirchhoff–Love equation in its second-order form in terms of q_θ. Both physics-informed loss terms are evaluated at collocation points $\mathbf{x}_{\mathrm{cp}} \in \Omega_C \subset \Omega$, and are composed of the MSE over all frequencies and collocation samples, as

$$\mathcal{L}_{\mathrm{aux}}(\theta) = \frac{1}{N_{\mathrm{f}}} \frac{1}{N_{\mathrm{cp}}} \sum_{i=1}^{N_{\mathrm{f}}} \sum_{j=1}^{N_{\mathrm{cp}}} \left| \nabla^2 w_\theta\left(f^{(i)}\right)\left(\mathbf{x}_{\mathrm{cp}}^{(i,j)}\right) - q_\theta\left(f^{(i)}\right)\left(\mathbf{x}_{\mathrm{cp}}^{(i,j)}\right) \right|^2, \tag{17}$$

$$\mathcal{L}_{\mathrm{PDE}}(\theta) = \frac{1}{N_{\mathrm{f}}} \frac{1}{N_{\mathrm{cp}}} \sum_{i=1}^{N_{\mathrm{f}}} \sum_{j=1}^{N_{\mathrm{cp}}} \left| \nabla^2 q_\theta\left(f^{(i)}\right)\left(\mathbf{x}_{\mathrm{cp}}^{(i,j)}\right) - \frac{\omega^2 \rho h}{D} w_\theta\left(f^{(i)}\right)\left(\mathbf{x}_{\mathrm{cp}}^{(i,j)}\right) \right|^2, \tag{18}$$

$$\mathcal{L}_{\mathrm{phys}}(\theta) = \mathcal{L}_{\mathrm{aux}}(\theta) + \mathcal{L}_{\mathrm{PDE}}(\theta). \tag{19}$$

The total loss function of the physics-informed DeepONet is then constituted as a weighted sum of the data-driven loss term $\mathcal{L}_{\mathrm{data}}$ in Eq. (15) and the physics-informed loss term $\mathcal{L}_{\mathrm{phys}}$ in Eq. (19), as

$$\mathcal{L}(\theta) = \mathcal{L}_{\mathrm{data}}(\theta) + \lambda\, \mathcal{L}_{\mathrm{phys}}(\theta), \tag{20}$$

where λ is a weighting hyperparameter that balances the trade-off between data fidelity and physical consistency. It is important to note that boundary conditions are enforced implicitly through the data-driven loss $\mathcal{L}_{\mathrm{data}}$. This implicit treatment is particularly beneficial for experimental cases, where the true boundary conditions are typically unknown or deviate from idealized assumptions. Rather than prescribing boundary conditions a priori, the DeepONet learns boundary behavior that is most consistent with the observed training data and the governing equations, thereby avoiding potentially incorrect idealized boundary constraints.

Furthermore, the Kirchhoff–Love plate equation in Eq. (18) is evaluated in its homogeneous form. This assumption is only valid when discrete point forces are considered and the location of the singularity is excluded from the set of collocation points in Ω_C. Moreover, it should be emphasized that the sampling of the training data points $\mathbf{x}_{\mathrm{tr}}$ and the collocation points $\mathbf{x}_{\mathrm{cp}}$ may vary for different frequencies $f^{(i)}$, thereby enabling frequency-adaptive sampling strategies and enhancing generalization capabilities across the spatial domain.

3.4. DeepONet architecture and implementation details

The DeepONet model employed in this study comprises two parallel feed-forward subnetworks: the branch network, which processes the input frequencies $f \in \mathbb{R}^{N_{\mathrm{f}}}$, and the trunk network, which takes the spatial coordinates $\mathbf{x} = [x, y] \in \mathbb{R}^2$ as inputs. A schematic overview of the physics-informed DeepONet architecture and the associated training workflow is depicted in Fig. 3. The left part of Fig. 3 shows the DeepONet architecture, with both subnetworks consisting of three fully-connected hidden layers with 80 neurons per layer. Residual skip connections are implemented between successive hidden layers to facilitate gradient flow. Sinusoidal activation functions are used throughout these studies, following the SIREN formulation [85], and the network weights are initialized accordingly using the SIREN-specific initialization scheme to ensure stable training [85]. The output dimension of the branch and the trunk network is set to $p = 100$. The final DeepONet output $\mathcal{G}_\theta(f)(\mathbf{x})$ is obtained by taking the inner product of the branch network feature vector $b_k = [b_1, b_2, \ldots, b_p]^T \in \mathbb{R}^p$ and the trunk network feature vector $t_k = [t_1, t_2, \ldots, t_p]^T \in \mathbb{R}^p$, cf. Eq. (13), followed by a linear projection layer. This output layer projects the combined inner product representation to four real-valued quantities: the real and imaginary parts of the transverse displacement field w_θ and its Laplacian $q_\theta = \nabla^2 w_\theta$, which serves as the auxiliary constraint in the second-order physics-informed loss formulation, see Eq. (16). This results in a four-dimensional output vector of the DeepONet illustrated in the center of Fig. 3, as

$$\mathcal{G}_\theta(f)(\mathbf{x}) \longrightarrow \left[\Re(w_\theta),\ \Im(w_\theta),\ \Re(q_\theta),\ \Im(q_\theta)\right]. \tag{21}$$

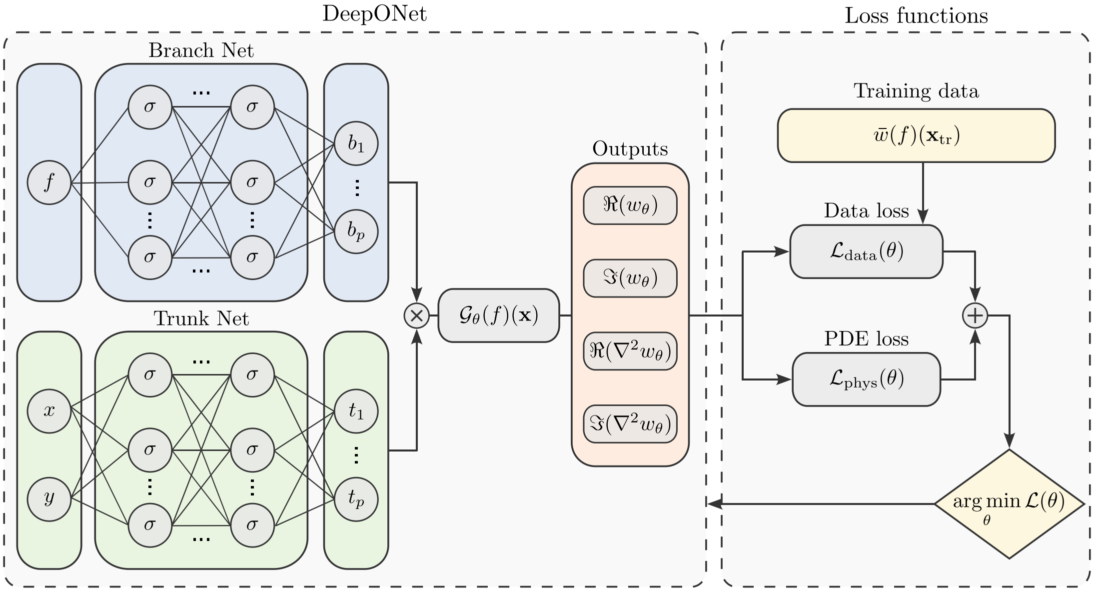

Fig. 3. Schematic illustration of a physics-informed DeepONet, consisting of the branch network and the trunk network (left). The DeepONet outputs (center) serve as the basis for computing the loss functions, comprised of the data-driven loss $\mathcal{L}_{\mathrm{data}}$, and the physics-informed loss $\mathcal{L}_{\mathrm{phys}}$ (right). The total loss function $\mathcal{L}(\theta)$, defined as the sum of the individual loss components, is minimized during training.

The right-hand side of Fig. 3 illustrates the construction of the loss functions. The total loss function $\mathcal{L}(\theta)$ consists of the data-driven loss $\mathcal{L}_{\mathrm{data}}(\theta)$, which penalizes discrepancies between the predicted displacements $w_\theta(f)(\mathbf{x})$ and the reference training data $\bar{w}(f)(\mathbf{x}_{\mathrm{tr}})$, cf. Eq. (15), and the physics-informed loss $\mathcal{L}_{\mathrm{phys}}(\theta)$, which enforces the Kirchhoff–Love plate equation in its second-order reformulation, as detailed in Eqs. (17)–(19). Both the real and imaginary components contribute additively to the MSE loss terms.

To enhance training stability and to ensure a proper balance between the data-driven and physics-based loss terms, two normalization steps are applied. First, for each frequency, the real and imaginary components of the displacement training data are normalized to the interval $[-1, 1]$ using frequency-wise min–max scaling computed from the respective training dataset. Second, the physics-informed loss $\mathcal{L}_{\mathrm{phys}}$ is normalized across all collocation points and frequencies within each batch to its initial value obtained after the first forward pass at the beginning of training. Together, these normalization steps ensure that both loss terms are on a comparable numerical scale, thereby preventing one term from dominating the total loss function even in cases of very small displacement amplitudes. This normalization scheme serves as a preparatory step for effective loss balancing, simplifying the selection of the weighting coefficient λ that controls the relative contribution of the two loss terms.

In the present study, a constant weighting factor of $\lambda = 0.1$ yielded the most stable convergence behavior, and the highest predictive accuracy. The optimal value of λ was determined through a grid-search optimization procedure. In addition, several adaptive balancing strategies have been implemented, including learning rate annealing [86], self-adaptive weighting [87], GradNorm [88], and ReLoBRaLo [89]. However, in this study involving only two non-competing loss terms, a constant weighting factor consistently provided better results than adaptive strategies. This may be attributed to the fact that adaptive balancing methods impose additional constraints on the optimization process, which can overconstrain the problem and divert optimization focus away from the primary objectives, resulting in less stable convergence.

Training is performed using the AdamW optimizer [90] with an initial learning rate of $\eta_{\mathrm{init}} = 10^{-3}$, a cosine annealing learning rate schedule with $\eta_{\mathrm{min}} = 10^{-4}$, and a weight decay of 10^{-5}. To further improve training stability, gradients are clipped to a maximum norm of 1.0. The model is trained for 30,000 epochs using batch-training with a batch size of 8192 for both the training data and the collocation points. Training data are reshuffled every epoch, and the model performance is monitored on a validation dataset at each epoch. All training routines are fully vectorized and optimized for usage on a graphics processing unit (GPU). The implementation is based on PyTorch [91], and the network architecture and hyperparameters have been optimized using a grid-search hyperparameter optimization.

During both the evaluation of the physical residuals in training and the assessment of DeepONet predictions during inference, the precomputed per-frequency scaling factors from the frequency-wise normalization are applied to rescale network outputs to physically consistent units. It should be noted that his study exclusively focuses on spatial generalization and does not target generalization across the frequency dimension. Accordingly, DeepONet predictions are evaluated at previously unseen spatial locations on the plate but only at the measured frequencies used for training. This restriction is methodologically motivated. Under frequency-wise normalization, no training data, and thus no scaling factors, exist for intermediate or out-of-band frequencies, making post hoc rescaling at interpolation or extrapolation frequencies infeasible. This choice is further supported by practical

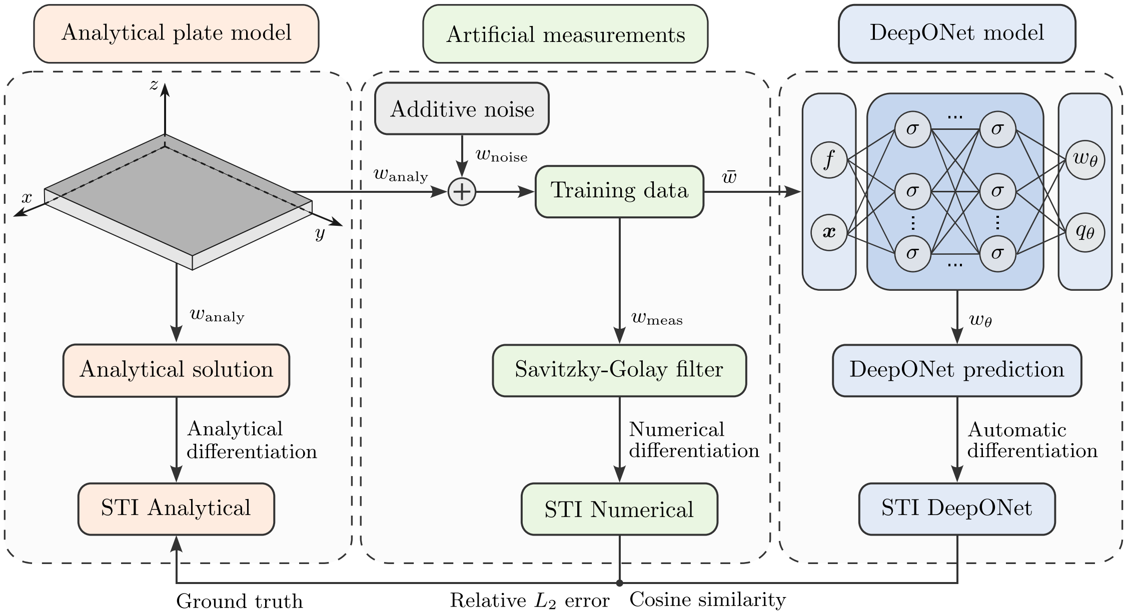

Fig. 4. Methodological overview for evaluating the DeepONet's predictive accuracy against an analytical plate model. The analytical solution (left) serves as the ground-truth reference, from which the STI is derived via analytical differentiation. Artificial measurement data (center), obtained by adding noise to the analytical solution, are used as training data for the DeepONet training. Numerical STI estimates are computed from the synthetic measurement data via numerical differentiation. In contrast, the DeepONet (right) learns a differentiable mapping, enabling STI prediction through automatic differentiation. The predictive accuracy of both the numerical and DeepONet-based STI estimates is evaluated against the analytical ground truth.

considerations. In STI applications, the relevant frequency range is typically specified a priori by the engineering task, e.g. structural resonances or excitation frequencies, and practical interest generally centers on the STI fields at those measured frequencies. Moreover, in LDV measurements, the dominant experimental effort is primarily imposed from dense spatial scanning rather than from increasing frequency resolution, particularly in the absence of a scanning LDV, thereby underlining the emphasis on spatial, rather than frequency, generalization.

4. Analytical plate example

As an initial demonstration of the proposed methodology, an analytical benchmark problem involving a simply supported rectangular plate is investigated. This test case is selected due to the availability of a closed-form analytical solution to the Kirchhoff–Love plate equation under the specific boundary conditions. The existence of an analytical reference allows for a rigorous and quantitative assessment of the predictive accuracy of the DeepONet-based surrogate model. In particular, it provides a reliable ground truth against which systematic error analyses and parameter studies can be conducted.

4.1. Methodological overview

Fig. 4 illustrates the methodological framework employed for error quantification and performance assessment using the analytical plate benchmark problem. As explained in Section 4.3, the reference solution is first obtained analytically from the Kirchhoff–Love plate model. From this analytical displacement field w_{analy}, the corresponding STI is derived via analytical differentiation, as depicted on the left side of the figure. This solution serves as the ground-truth reference for the subsequent evaluations. To simulate realistic measurement conditions, additive Gaussian noise w_{noise} is applied to the analytical displacement data, resulting in artificial measurements w_{meas} that emulate imperfections typically observed in experimental settings, as shown in the center panel of Fig. 4. The artificial measurement data are used in two ways. First, the STI is estimated numerically by applying finite-difference-based differentiation of the noisy displacement field. Second, the noisy data serve as training input for the DeepONet model.

Prior to numerical differentiation, the noisy displacement data w_{meas} are smoothed using a Savitzky–Golay filter [74] to enhance the accuracy of the derivative estimates. The Savitzky–Golay filter is a digital smoothing filter that fits a low-degree polynomial to a symmetric moving window of the data using a least-squares approach [74]. From this polynomial fit, both the smoothed values and their derivatives at the central point can be evaluated. In this work, a third-order polynomial and a window size of seven points are used. This method has demonstrated robust performance when applied to LDV measurement data [14,92] and is widely regarded as a state-of-the-art technique for estimating strain fields via numerical differentiation of noisy experimental data [93,94].

The right part of the figure illustrates the physics-informed DeepONet model, as described in Section 3.3. Once trained, this model provides a continuously differentiable mapping from input coordinates and frequency to the displacement solution, allowing for the computation of the STI via automatic differentiation. The proposed framework thus enables a rigorous comparison of three complementary approaches to STI estimation: analytical differentiation of the exact solution, numerical differentiation of noisy synthetic measurements, and automatic differentiation of the DeepONet prediction.

The predictive performance of the DeepONet model is quantitatively assessed using two complementary error measures: the relative L_2 error, which captures discrepancies in amplitude, and the cosine similarity, which evaluates directional agreement between vector fields. Both metrics are computed with respect to the analytical ground truth solution. Given a predicted STI vector field $\mathbf{I}_{\text{pred}}$ and the analytical reference STI vector $\mathbf{I}_{\text{ref}}$, the L_2 error is defined as

$$L_2 = \frac{\left\| |\mathbf{I}_{\text{ref}}| - |\mathbf{I}_{\text{pred}}| \right\|_2}{\left\| \mathbf{I}_{\text{ref}} \right\|_2} = \sqrt{\frac{\sum_{i=1}^{N_{\text{eval}}} \left| |\mathbf{I}_{\text{ref}}(\mathbf{x}_i)| - |\mathbf{I}_{\text{pred}}(\mathbf{x}_i)| \right|^2}{\sum_{i=1}^{N_{\text{eval}}} \left| \mathbf{I}_{\text{ref}}(\mathbf{x}_i) \right|^2}}, \tag{22}$$

where $\|\cdot\|_2$ denotes the L_2 norm, $|\mathbf{I}_{\text{ref}}|$ and $|\mathbf{I}_{\text{pred}}|$ refer to the complex-valued STI magnitudes, cf. Eq. (8), and N_{eval} is the total number of spatial evaluation points. To quantify directional agreement between the vector fields, the cosine similarity is employed, defined as

$$\text{Cos Sim} = \frac{\left\langle \mathbf{I}_{\text{ref}}, \mathbf{I}_{\text{pred}} \right\rangle}{\left\| \mathbf{I}_{\text{ref}} \right\|_2 \cdot \left\| \mathbf{I}_{\text{pred}} \right\|_2}, \tag{23}$$

where $\langle \cdot, \cdot \rangle$ denotes the dot product of the flattened vector fields. A cosine similarity value of $\text{Cos Sim} = 1$ indicates perfect directional alignment, while lower values reflect increasing angular deviation. A value of $\text{Cos Sim} = -1$ corresponds to complete directional opposition.

4.2. Plate model description

The plate model considered in this study is a well-established benchmark problem in STI literature, originally introduced by Gavrić and Pavić [24], and subsequently adopted in several studies for model verification and comparison [28,29]. The plate model consists of a rectangular, simply supported Kirchhoff–Love plate subjected to a sinusoidal point force excitation and equipped with a viscous point damper. To ensure direct comparability, the geometric dimensions, boundary conditions, material properties, and loading configurations are identical to those in [24]. The plate dimensions in x- and y-direction are $a \times b = 3\,\text{m} \times 1.7\,\text{m}$ with a uniform thickness of $t = 1\,\text{cm}$. The material is assumed to be linear elastic, with Young's modulus $E = 210\,\text{GPa}$, Poisson's ratio $\mu = 0.3$, and mass density $\rho = 7800\,\text{kg/m}^3$. The plate is excited by a vertical, time-harmonic point force of amplitude $F_0 = 1000\,\text{N}$, applied over a frequency range of $f = 10$ - $80\,\text{Hz}$ in increments of $1\,\text{Hz}$. The excitation is located at $[x_F = 0.6\,\text{m},\ y_F = 0.4\,\text{m}]$, measured from the lower-left corner of the plate. A viscous point damper with the damping coefficient of $d = 100\,\text{Ns/m}$ is attached to the plate at $[x_D = 2.2\,\text{m},\ y_D = 1.2\,\text{m}]$. The plate geometry, along with the locations of the excitation force and damper, is depicted in Fig. 5.

4.3. Analytical solution of a simply supported plate

The analytical reference solution for a simply supported, undamped Kirchhoff–Love plate is derived via modal decomposition of the dynamic response, following the approach by Gavrić and Pavić [24]. This formulation enables a closed-form solution of the transverse displacement field $w_{\text{analy}}(\mathbf{x})$ by summing the contributions of individual vibration modes as a truncated modal expansion. The natural angular frequencies ω_{nm} of the undamped system are given by

$$\omega_{nm} = \sqrt{\frac{Dab}{M}} \left(\left(\frac{n\pi}{a} \right)^2 + \left(\frac{m\pi}{b} \right)^2 \right), \quad n, m \in \mathbb{N}, \tag{24}$$

where D is the flexural rigidity, $M = \rho hab$ is the total plate mass, a, b and t denote the plate dimensions, and n, m are the respective mode numbers. The mode shapes $\Phi_{nm}(x, y)$ satisfying simply supported boundary conditions are expressed as

$$\Phi_{nm}(x, y) = 2 \sin\left(\frac{n\pi x}{a} \right) \sin\left(\frac{m\pi y}{b} \right). \tag{25}$$

The complex-valued transverse displacement field $w_{\text{analy}}(\mathbf{x})$ is obtained by truncated modal superposition, as

$$w_{\text{analy}}(\mathbf{x}) = \frac{1}{M} \sum_{n=1}^{N} \sum_{m=1}^{M} \Gamma_{nm}(\omega) \Phi_{nm}(x, y), \tag{26}$$

where the modal participation factor $\Gamma_{nm}(\omega)$ that incorporates the effects of the external point force and the damper are given by

$$\Gamma_{nm}(\omega) = \frac{F_0 \Phi_{nm}(x_F, y_F) + \tilde{R}(\omega) \Phi_{nm}(x_z, y_z)}{\omega_{nm}^2 - \omega^2}. \tag{27}$$

The complex-valued reaction force of the damper $\tilde{R}(\omega)$ is derived from the coupled modal response and takes the form

$$\tilde{R}(\omega) = -\mathrm{i}\omega d F_0 \frac{\sum_{n=1}^{N} \sum_{m=1}^{M} \frac{\Phi_{nm}(x_F, y_F) \Phi_{nm}(x_z, y_z)}{\omega_{nm}^2 - \omega^2}}{M + \mathrm{i}\omega d \sum_{n=1}^{N} \sum_{m=1}^{M} \frac{\Phi_{nm}^2(x_z, y_z)}{\omega_{nm}^2 - \omega^2}}, \tag{28}$$

Table 1

First ten eigenfrequencies f_{nm} in Hz of a simply supported rectangular plate with the dimensions and material properties, as specified in Section 4.2.

Mode (n, m)	(1,1)	(2,1)	(3,1)	(1,2)	(2,2)	(4,1)	(3,2)	(5,1)	(4,2)	(1,3)
Eigenfrequency f_{nm} in Hz	11.27	19.50	33.20	36.88	45.10	52.38	58.80	77.05	77.99	79.55

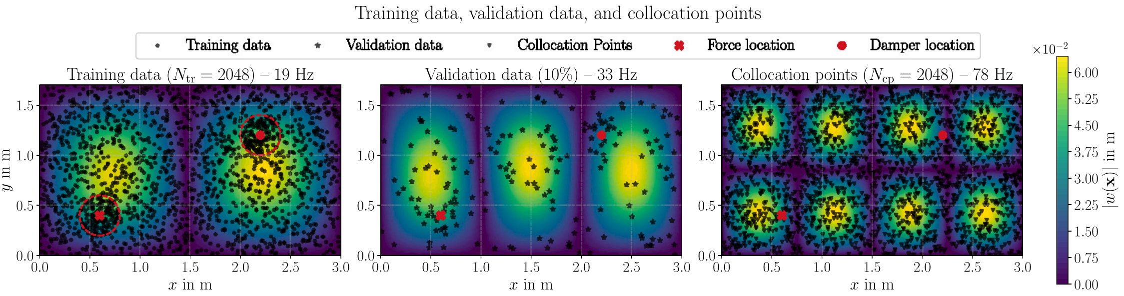

Fig. 5. Visualization of the spatial distribution of training data, validation data, and collocation points used for the physics-informed DeepONet based on the analytical plate example. The locations of the point excitation and damping are indicated, with circular regions in the training data plot highlight the areas of refined sampling around the singularities. Analytical displacement fields are shown at selected frequencies close to eigenfrequencies of the plate.

where d denotes the viscous damping coefficient and F_0 is the amplitude of the harmonic excitation.

In this study, the modal series is truncated to $N = M = 30$ for computational feasibility, which has been verified to yield accurate approximations of the transverse displacement field across the frequency range of interest [24]. To assess the accuracy of the implemented modal formulation and verify consistency with published reference data, the first ten eigenfrequencies, defined as $f_{nm} = \omega_{nm}/(2\pi)$, are computed and listed in Table 1. The obtained values are in exact agreement with those reported in Gavrić and Pavić [24], thereby confirming the validity of the implemented analytical solution.

The analytical solution given in Eq. (26) serves as the ground-truth reference for evaluating the predictive performance of the DeepONet surrogate model. The STI field is derived in a post-processing step from the analytical displacement field according to Eq. (7). In this special case, where a closed-form analytical solution is available, the spatial derivatives required in Eq. (7) are obtained through direct analytical differentiation of the modal series in Eq. (26), thereby ensuring maximal precision in the STI reference computation.

4.4. Training data generation and collocation point sampling

The training and validation datasets used to train the DeepONet are generated based on the analytical solution of the Kirchhoff–Love plate model described in Section 4.3. To generate the training data, for each frequency f in the range $10\,\mathrm{Hz} \le f \le 80\,\mathrm{Hz}$ with a resolution of $\Delta f = 1\,\mathrm{Hz}$, synthetic data are computed by evaluating the complex-valued displacement field $w(\mathbf{x}, f)$ at spatial positions $\mathbf{x} \in \Omega$, where $\Omega = [0, a] \times [0, b]$ denotes the plate domain. This frequency range is chosen to fully capture the first ten eigenfrequencies of the system, see Table 1, which represent the most dominant vibration modes of the plate.

To sample the spatial input locations for each frequency, Latin Hypercube Sampling (LHS) is employed using fixed random seeds to ensure reproducibility. Specifically, $N_{\mathrm{tr}} = 2048$ training points are generated per frequency, of which 1792 points are sampled uniformly over the entire spatial domain using standard LHS. To increase sampling density near singularities caused by the point force and point damper, an additional 2×128 points are sampled within circular regions of radius $0.2\,\mathrm{m}$ centered at the respective singularities using a refined LHS scheme. The resulting spatial distribution of the training data for training frequency close to an eigenfrequency is shown in the left panel of Fig. 5.

The validation dataset is constructed by randomly selecting 10% of the available training points without replacement, ensuring disjoint validation samples, as illustrated in the middle plot of Fig. 5. The displacement field $w(\mathbf{x}, f)$ is evaluated analytically at all training and validation points.

To simulate realistic measurement conditions, zero-mean Gaussian noise is added to the training data. The noise level is adjusted individually for each frequency based on a specified signal-to-noise ratio (SNR) in dB, and the noise is applied independently to the real and imaginary parts of the displacement field. A detailed investigation of the effects of SNR and training set size is provided in Sections 4.8 and 4.9.

To evaluate the physics-based residuum in Eq. (18), a separate set of $N_{\mathrm{cp}} = 2048$ collocation points $\mathcal{D}_{\mathrm{cp}} = \{(f_{\mathrm{cp}}, \mathbf{x}_{\mathrm{cp}})\}$ is generated using LHS over the joint frequency-spatial domain $\mathcal{F}_C \times \Omega_C$, with $\mathcal{F}_C$ being the space of collocation frequencies. To prevent numerical instabilities near the singularities induced by the point excitation and damping, samples within a fixed exclusion radius of $0.05\,\mathrm{m}$ of these locations are discarded.

After data generation, all spatial coordinates $\mathbf{x}$ and frequencies f are normalized to the range $[-1, 1]$ using global linear min–max scaling. Furthermore, frequency-wise normalization is applied to the real and imaginary parts of the complex-valued displacement

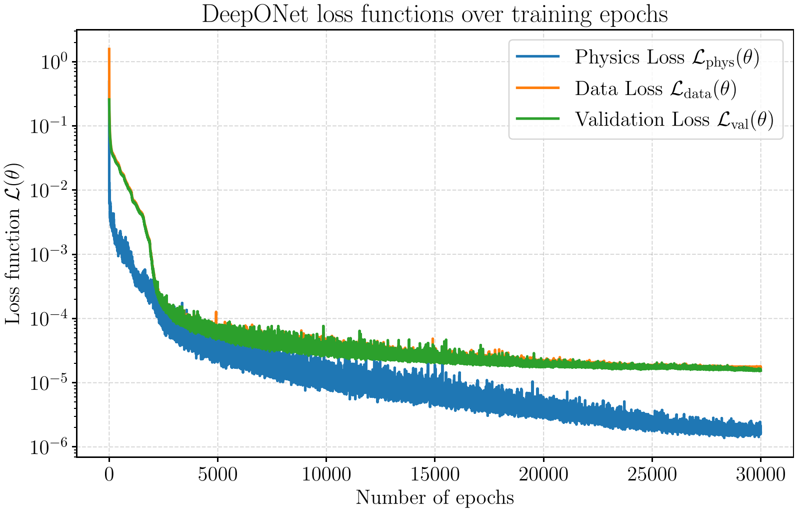

Fig. 6. Evolution of the training loss functions during DeepONet training based on the analytical plate solution, plotted over the number of training epochs. The individual loss components, namely physics loss $\mathcal{L}_{\text{phys}}$, data loss $\mathcal{L}_{\text{data}}$, and validation loss $\mathcal{L}_{\text{val}}$ are displayed separately to illustrate their respective convergence behavior throughout the training process. Color legend: blue = physics loss $\mathcal{L}_{\text{phys}}$, orange = data loss $\mathcal{L}_{\text{data}}$, green = validation loss $\mathcal{L}_{\text{val}}$.

data, using the minimum and maximum values computed from the training set at each frequency. The collocation points are normalized using the same min–max scaling as applied to the training data. These scaling factors are stored and reused for consistent rescaling of the prediction during model inference.

4.5. Training convergence and loss evolution

Following the training procedure of the physics-informed DeepONet using the dataset and architecture described in Sections 3.4 and 4.4, the convergence behavior of the individual loss terms is illustrated in Fig. 6. The plot displays the evolution of the individual loss terms, namely the data-driven loss $\mathcal{L}_{\text{data}}$, the physics-informed loss $\mathcal{L}_{\text{phys}}$, and the validation loss $\mathcal{L}_{\text{val}}$, plotted over the number of training epochs on a logarithmic scale. All three loss functions exhibit consistent and monotonic convergence behavior over several orders of magnitude, indicating stable and effective training convergence. The close agreement between the data-driven $\mathcal{L}_{\text{data}}$ and validation loss $\mathcal{L}_{\text{val}}$ curves demonstrates strong generalization capabilities without overfitting throughout the training process. Additionally, the physics-informed loss $\mathcal{L}_{\text{phys}}$ is further reduced during training, reaching values below a MSE of 10^{-5}, confirming that the learned DeepONet solution satisfies the governing Kirchhoff–Love plate equation with high precision. Notably, the loss functions become increasingly smooth over the course of training, indicating proper loss balancing and effective physics-informed regularization.

4.6. DeepONet displacement prediction

After training the physics-informed DeepONet as outlined in Section 4.5, the model is capable of predicting the real and imaginary parts of the transverse displacement field $w(f)(\mathbf{x})$ governed by the Kirchhoff–Love plate equation for arbitrary spatial locations $\mathbf{x} \in \Omega$ and frequencies $f \in \mathcal{F}$ within the training range, as described in Section 3.3. For the subsequent studies, the DeepONet predictions and reference methods are evaluated on a uniform 80×80 spatial grid during the inference stage. The predicted values are rescaled to the physical quantities using the precomputed scaling factors, as described in Section 4.4. This evaluation is performed exclusively at unseen test points that were not included in the training data, ensuring an unbiased assessment of predictive performance on pure generalization data.

Fig. 7 presents the results of the displacement field at a frequency of 50 Hz, which is selected for comparability in accordance with the benchmark studies presented in [24]. The analytical reference solution is shown in the left column, while the DeepONet prediction is displayed in the middle column. The top and bottom rows depict the real and imaginary parts of the displacement field, respectively. The right column depicts the pointwise absolute error between prediction and reference, along with the corresponding mean absolute error (MAE) as a quantitative error measure.

The DeepONet yields highly accurate predictions, achieving MAE values in the order of 10^{-6} for the real part and 10^{-9} for the imaginary part. These results confirm that both the amplitude and the spatial distribution of the displacement field are captured with high precision, achieving excellent agreement with the analytical reference. The error plots indicate that the largest absolute errors occur in the vicinity of the singularities associated with the excitation force and the damper, where the displacement gradients are highest. In particular, the largest errors in the real part are located near the force, which contributes a real-valued term to the

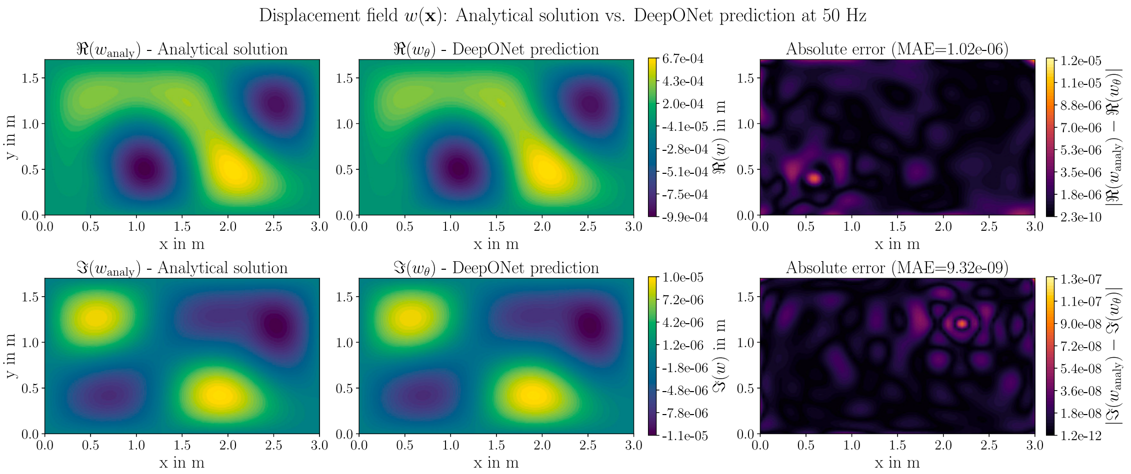

Fig. 7. Comparison between the transversal displacement field $w(\mathbf{x})$ of the analytical reference solution and the DeepONet prediction at a frequency of 50 Hz. The real part $\Re(w)$ and imaginary part $\Im(w)$ of the displacement field are shown separately, along with a field plot of the absolute error between the DeepONet prediction and the analytical reference. The mean absolute error (MAE) is also provided as a quantitative measure of prediction accuracy.

displacement solution, cf. Eq. (27). In contrast, the imaginary part exhibits the largest errors near the damper location, consistent with the purely imaginary reaction force introduced by the damper, see Eq. (28).

Across the entire frequency range used during training, the physics-informed DeepONet consistently demonstrates high predictive accuracy. As illustrated in Fig. 9(a), the relative L_2 error remains below 10^{-2} for all evaluated frequencies, with a mean value of 4.40×10^{-3}. These results underline the effectiveness and generalization capabilities of the proposed DeepONet architecture for predicting the frequency-dependent displacement response of the analytical Kirchhoff–Love plate model.

4.7. DeepONet structural intensity prediction

The physics-informed DeepONet has demonstrated excellent accuracy in predicting the complex-valued transverse displacement field w_θ in Section 4.6. Building upon this, the STI field is derived from the predicted displacement field w_θ and q_θ. As illustrated in the right part of Fig. 4, the STI is derived via automatic differentiation from the DeepONet outputs. In this process, the definition of the auxiliary variable $q_\theta = \nabla^2 w_\theta$, cf. Eq. (16), is substituted into the displacement-based formulation of the STI in Eq. (7). This substitution reduces the required third-order derivatives for computing the shear forces, cf. Eq. (5), to a first-order derivative of q_θ, thereby improving numerical stability and computational efficiency.

Fig. 8 provides a detailed comparison between the STI fields predicted by the DeepONet and the two reference approaches with a noise SNR level of 40 dB, as summarized in Fig. 4. The normalized STI magnitude $|\mathbf{I}|$ is visualized as a color map, while the directional characteristics of the STI vector field $\mathbf{I} = [I_x, I_y]$ are represented by arrow plots. The left column shows the analytical reference solution, the middle column depicts the DeepONet prediction, and the right column displays a finite-difference-based STI estimate using Savitzky–Golay filtering and numerical differentiation. The numerical differentiation procedure requires displacement data sampled on a regular spatial grid. As outlined in Section 4.6, all STI evaluations are performed on a uniform grid comprising 80 × 80 spatial points. It should be noted that the numerically differentiated results are thus based on a denser dataset (6400 points in total) than the DeepONet training data, which includes $N_{\mathrm{tr}} = 2048$ samples, cf. Section 4.4. Using a grid with lower spatial resolution for numerical differentiation results in substantially larger errors. To ensure comparability across all methods, a consistent regular 80 × 80 grid is employed for all evaluation methods.

Each row in Fig. 8 corresponds to a selected frequency, chosen to highlight characteristic features of the vibrational energy flow. To quantitatively assess the predictive performance, each subplot includes the mean relative L_2 error and the averaged cosine similarity between the predicted and the analytical STI fields. Fig. 8 presents the predicted STI fields across five different excitation frequencies, arranged in rows. The first three rows correspond to frequencies near the first three eigenfrequencies of the plate, as listed in Table 1. The fourth row shows the STI field at the benchmark frequency of 50 Hz, allowing direct comparison with the benchmark study in Ref. [24]. The bottom row depicts the STI field at 77 Hz, which coincides with the eigenfrequency of mode (5, 1).

Overall, the DeepONet predictions show good agreement with the analytical ground truth across all frequencies. Both the magnitude distribution and the vector directionality of the normalized STI fields are well captured by the DeepONet model. The lowest directional agreement is observed at 11 Hz, with a cosine similarity of 0.79, while the highest agreement is achieved at 77 Hz, reaching a cosine similarity of 0.99. The corresponding relative L_2 errors range from 4.45×10^{-1} to 7.18×10^{-2}. Notably, the STI estimation derived via numerical differentiation of the Savitzky–Golay filtered displacement data, shown on the right of Fig. 8, show significantly lower accuracy than the DeepONet predictions.

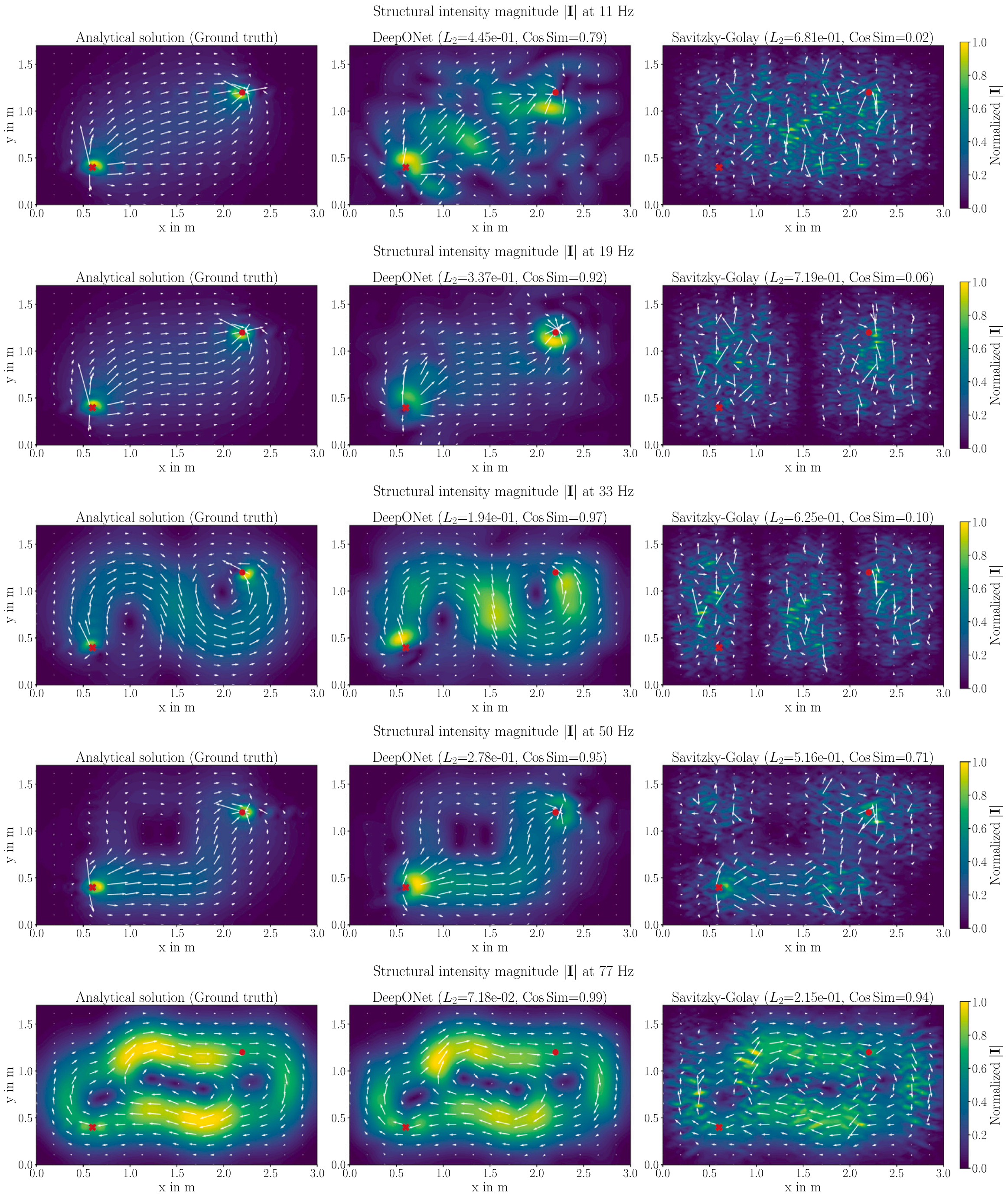
Structural intensity magnitude $|\mathbf{I}|$ at 11 Hz

Analytical solution (Ground truth) DeepONet (L_2=4.45e-01, Cos Sim=0.79) Savitzky-Golay (L_2=6.81e-01, Cos Sim=0.02)

Structural intensity magnitude $|\mathbf{I}|$ at 19 Hz

Analytical solution (Ground truth) DeepONet (L_2=3.37e-01, Cos Sim=0.92) Savitzky-Golay (L_2=7.19e-01, Cos Sim=0.06)

Structural intensity magnitude $|\mathbf{I}|$ at 33 Hz

Analytical solution (Ground truth) DeepONet (L_2=1.94e-01, Cos Sim=0.97) Savitzky-Golay (L_2=6.25e-01, Cos Sim=0.10)

Structural intensity magnitude $|\mathbf{I}|$ at 50 Hz

Analytical solution (Ground truth) DeepONet (L_2=2.78e-01, Cos Sim=0.95) Savitzky-Golay (L_2=5.16e-01, Cos Sim=0.71)

Structural intensity magnitude $|\mathbf{I}|$ at 77 Hz

Analytical solution (Ground truth) DeepONet (L_2=7.18e-02, Cos Sim=0.99) Savitzky-Golay (L_2=2.15e-01, Cos Sim=0.94)

Fig. 8. Comparison of STI fields obtained from the analytical reference solution (left column), the DeepONet prediction (middle column), and numerical differentiation using Savitzky–Golay filter (right column). Each subplot displays the normalized STI magnitude $|\mathbf{I}|$ along with the STI vector fields $[I_x, I_y]$, indicating the STI direction. Results are presented for selected frequencies (in each row), as indicated in the titles of each subplot and a SNR of 40 dB. Quantitative evaluation of prediction accuracy is provided in terms of relative L_2 error and cosine similarity. The position of the point force excitation and the dampers are marked with a red cross and a red dot, respectively.

While the basic features of the STI patterns are partially recovered at 50 Hz and 77 Hz, the results are visibly affected by pronounced artifacts, such as vertical stripe patterns and strong localized distortions introduced by numerical differentiation instabilities. At frequencies close to the first three eigenfrequencies, numerical differentiation fails entirely, producing STI fields that diverge significantly from the analytical reference. This observation is consistent with known limitations reported in STI literature

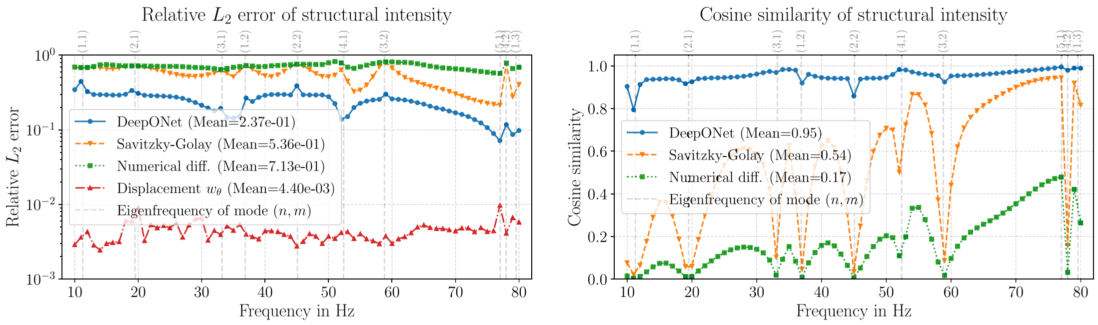

(a) Relative L_2 error as a function of frequency.

(b) Cosine similarity as a function of frequency.

Fig. 9. Frequency-dependent error analysis of the STI predictions using two error metrics: The relative L_2 error (left) for the magnitude error and cosine similarity (right) for the directional error. Color legend: blue = DeepONet prediction, orange = Savitzky–Golay filtered numerical differentiation, green = numerical differentiation without prior filtering, red = relative L_2 error of the DeepONet displacement field w, gray = analytical eigenfrequencies of the plate with corresponding mode numbers. All errors are evaluated with respect to the analytical reference solution.

and is attributed to resonance-induced amplification effects. Near resonances, the displacement amplitudes become large, resulting in steep spatial gradients, which amplify discretization errors and instability in the differentiation process. Interestingly, the spatial patterns of the artifacts in the numerically differentiated STI fields roughly reflect the corresponding mode shapes. For instance, the pattern at 11 Hz resembles mode $(1, 1)$, at 19 Hz mode $(2, 1)$, and at 33 Hz mode $(3, 1)$, see Table 1 for reference.

In summary, the proposed DeepONet approach clearly outperforms the state-of-the-art numerical differentiation method with Savitzky–Golay filtering, both in representing the magnitude distribution and the vector directionality of the predicted STI fields. Whereas numerical differentiation breaks down in the vicinity of eigenfrequencies due to resonance-driven numerical instabilities, the DeepONet model continues to provide reliable and accurate predictions. It is important to emphasize that the cosine similarity metric provides a more appropriate error measure for evaluating STI fields than the magnitude-based relative L_2 norm, as the relative L_2 error can be strongly affected by localized amplitude mismatches near singularities. This can lead to relatively high L_2 errors, even though the overall directional STI patterns are accurately captured.

Fig. 9 shows the spatially averaged error metrics of the different STI prediction methods as a function of frequency across the examined frequency range. Specifically, Fig. 9(a) displays the relative L_2 error, while Fig. 9(b) depicts the cosine similarity. The results compare the performance of the physics-informed DeepONet, numerical differentiation with Savitzky–Golay filtering, and unfiltered numerical differentiation, each evaluated against the analytical reference solution. Moreover, Fig. 9(a) includes the relative L_2 error of the DeepONet-predicted displacement field $w_\theta(f)$, providing further insight into the model's predictive accuracy over the frequency range. For reference, the eigenfrequencies of the plate and their associated mode numbers, see Table 1, are indicated along the top of the plots. Frequency-averaged error values are reported quantitatively to facilitate direct comparison across methods.

A detailed examination of the results in Fig. 9 demonstrates that the DeepONet consistently outperforms both numerical differentiation approaches across the entire frequency range, as measured by both the relative L_2 error and cosine similarity. The improvement is particularly pronounced at low frequencies, where the DeepONet achieves substantially higher cosine similarity values compared to the other two methods. Among the two numerical differentiation approaches, the application of Savitzky–Golay filtering leads to a clear and consistent improvement in prediction accuracy over unfiltered differentiation across all frequencies. In terms of amplitude errors, the relative L_2 error of the DeepONet-predicted displacement field $w_\theta(f)$ is approximately two orders of magnitude lower than that of the derived STI field, reflecting the error amplification introduced by the differentiation process.

Across both error metrics, sharp drops in accuracy are observed at the frequencies close to the plate's eigenfrequencies, which are more pronounced for the numerically differentiated STI predictions than for the DeepONet. As previously discussed, this effect results from resonance-induced amplification of displacement amplitudes and their spatial gradients, which leads to numerical instability and increases discretization errors. Fig. 9(b) further supports the reasoning for selecting the representative frequencies shown in Fig. 8. The frequency of 11 Hz marks the worst-case scenario with the lowest cosine similarity values for the DeepONet prediction of a value below 0.8, while 77 Hz corresponds to the most accurate predictions for both DeepONet and the Savitzky–Golay method. Across the other eigenfrequencies, the DeepONet consistently achieves significantly higher predictive accuracy, clearly demonstrating the robustness and effectiveness of the proposed data-driven, physics-informed framework over conventional numerical differentiation techniques.

4.8. Parameter study on the number of training data

To assess the applicability of the proposed DeepONet framework, it is essential to investigate the impact of training dataset size on prediction accuracy. For this purpose, a parameter study is conducted using the analytical plate model, where only the number of training data samples N_{tr} per frequency is varied, while all other settings remain unchanged. The DeepONet architecture

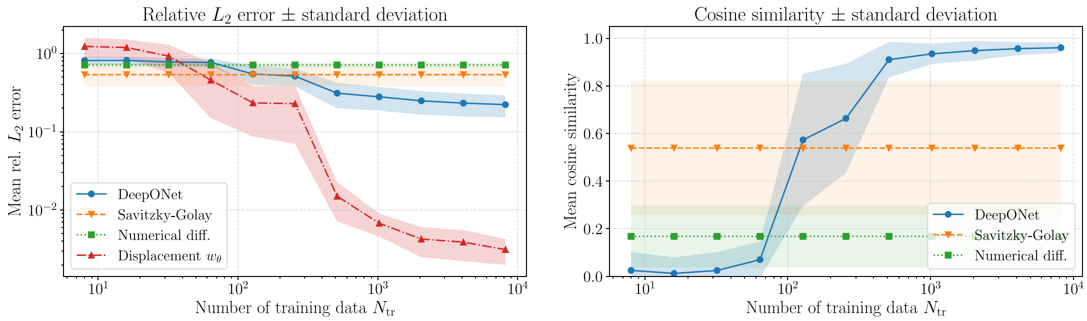

(a) Mean relative L_2 error as a function of the number of training data samples N_{tr}.

(b) Mean cosine similarity as a function of the number of training data samples N_{tr}.

Fig. 10. Results of the parameter study investigating the influence of the training data quantity on DeepONet performance. The left plot shows the mean relative L_2 error for the predicted STI field and the DeepONet displacement field approximation, while the right plot presents the mean cosine similarity of the STI predictions. Shaded regions indicate one standard deviation around the mean. Color legend: blue = DeepONet STI prediction, red = DeepONet displacement field approximation, orange = Savitzky–Golay filtered numerical differentiation, green = numerical differentiation without filtering. The numerical differentiation results, evaluated on the full grid, are independent of the number of training samples and shown for reference.

and training configuration follow the specifications detailed in Sections 3.4 and 4.4, and the SNR is fixed at 40 dB. The number of training samples is increased systematically from 8 to 8192 in powers of two, a step size chosen to optimize training efficiency on GPU hardware. The analytical displacement solution and STI fields are used as reference solutions, and errors are computed as mean values averaged over space and frequency. The results of this study are summarized in Fig. 10.

The relative L_2 error and cosine similarity are plotted as functions of training set size in Figs. 10(a) and 10(b), respectively. As in Fig. 11, the DeepONet predictions are compared to numerically differentiated STI estimates with and without Savitzky–Golay filtering. However, in this study the numerical results serve solely as reference baselines, as they are computed on the full spatial grid and are therefore independent of the DeepONet training data size.

The results clearly indicate that increasing the number of training samples generally improves the accuracy of the STI prediction. As shown in Fig. 10(b), for very small datasets ($N_{tr} < 32$ samples), DeepONet underperforms relative to the numerical baselines, which are however computed on the full spatial 80 × 80 grid with 6400 data points, as detailed in Section 4.6. A notable improvement occurs from 128 samples onward, where DeepONet begins to outperform both numerical methods in terms of cosine similarity. A similar trend is evident in the relative L_2 error of the displacement field, cf. Fig. 10(a), where a clear improvement in prediction quality occurs starting at 256 training samples. When looking at the uncertainty range in Section 4.6, the standard deviation of the cosine similarity decreases with increasing training data size, confirming the stability and convergence of the proposed methodology.

These findings suggest that at least 1024 training data samples are required to achieve high-fidelity predictions, characterized by a relative L_2 error below 1×10^{-2} and a cosine similarity above 0.9. The results also reveal that increasing the dataset beyond 2048 samples yields only marginal accuracy improvements. Thus, the 2048 sample configuration used in Section 4.4 offers an effective trade-off between accuracy and computational costs. This study also highlights the inherent trade-off between training time and prediction accuracy. For reference, training the DeepONet for 30,000 epochs with a constant batch size on a NVIDIA GeForce RTX 5080 GPU requires 6 h 5 min with 2048 samples, while training with 1024 and 512 samples takes only 4 h 49 min and 2 h 19 min, respectively. These results emphasize the need to balance accuracy requirements with available computational resources when selecting the right problem-specific training dataset size.

4.9. Parameter study on the SNR within the training data

To further evaluate the robustness of the proposed methodology under realistic experimental conditions, it is essential to assess its sensitivity to noise in the training data. For this purpose, a parameter study is conducted using the analytical plate model, in which the SNR of the additive Gaussian noise is systematically varied from 5 to 60 dB. The analytical solution of the displacement field and the analytically derived STI field serve as the ground-truth reference throughout the study.

Fig. 11 summarizes the results of this study. Specifically, Fig. 11(a) shows the spatially and frequency-averaged relative L_2 error of both the predicted displacement field and the resulting STI, while Fig. 11(b) displays the corresponding averaged cosine similarity, both as functions of the SNR. For each method, mean values and associated uncertainty regions are plotted, represented as shaded regions with one standard deviation around the mean value. The DeepONet predictions are compared against those obtained via numerical differentiation with and without Savitzky–Golay filtering applied to the noisy displacement data.

The results clearly demonstrate that prediction accuracy generally improves with increasing SNR (decreasing noise levels) across all methods. Both the displacement and STI predictions exhibit asymptotic convergence behavior as SNR increases. Notably, the DeepONet consistently outperforms both numerical differentiation approaches in high-noise regimes (low SNR), as reflected by

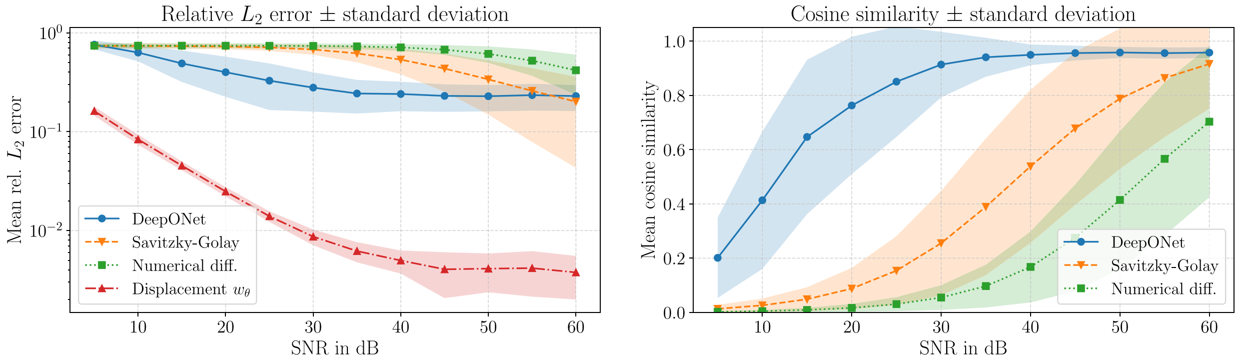

(a) Mean relative L_2 error as a function of the SNR of the noise.

(b) Mean cosine similarity as a function of the SNR of the noise.

Fig. 11. Results of the SNR parameter study on the noise level of the additive Gaussian noise. The left plot shows the mean relative L_2 error of the STI predictions, while the right plot displays the mean cosine similarity, both as functions of the SNR level of the added noise. Shaded regions indicate the uncertainty range of one standard deviation around the mean. Color legend: blue = DeepONet prediction, orange = Savitzky–Golay filtered numerical differentiation, green = numerical differentiation without filtering, red = relative L_2 error of the DeepONet-predicted displacement field w.

significantly higher cosine similarity values in Fig. 11(b). This finding supports the initial hypothesis that data-driven neural network models are inherently more robust to noise than conventional numerical techniques, cf. [45].

Moreover, the standard deviation of the DeepONet predictions decreases with increasing SNR, further highlighting the stability of the approach. In contrast, the uncertainty in the numerically differentiated results increases with SNR, indicating higher sensitivity to noise-induced gradient fluctuations. While Savitzky–Golay filtering offers a clear improvement over unfiltered differentiation, DeepONet consistently achieves higher directional accuracy across all noise levels. Even at an SNR of 60 dB, where the signal is very clean, DeepONet predicts the STI with a cosine similarity above 0.95.

In terms of amplitude-based error, Fig. 11(a) shows that the relative L_2 error of the Savitzky–Golay-based STI estimation falls slightly below the DeepONet at 60 dB SNR. However, as discussed in Section 4.7, the cosine similarity is a more appropriate metric for assessing STI field accuracy, as it captures directional agreement and is less affected by local amplitude mismatches near singularities. Accordingly, the directional accuracy of the DeepONet remains the more relevant indicator of predictive performance.

Overall, the study indicates that the proposed DeepONet-based approach delivers reliable STI predictions at SNR levels of 30 dB and above. At this noise level, the mean relative L_2 error of the predicted displacement field falls below 1×10^{-2}, and the cosine similarity of the STI prediction exceeds 0.9. These values fall within typical experimental noise conditions, supporting the applicability of the DeepONet framework to real-world measurement data.

4.10. Comparison between purely data-driven and physics-informed DeepONets

To assess the effect of incorporating physics-based loss terms on predictive accuracy, a comparative study is conducted between a physics-informed DeepONet and a purely data-driven DeepONet. This analysis aims to quantify the benefits of incorporating physical constraints, with particular emphasis on the high-noise regime and the dependence of model performance on the SNR of the training data. To ensure a fair comparison, the network architecture, all hyperparameters, cf. Section 3.4, as well as the training data and collocation points, cf. Section 4.4, are kept identical to those used for the physics-informed model. The only modification is that, during the training of the purely data-driven DeepONet, only the data-driven loss term $\mathcal{L}_{\text{data}}$ in Eq. (20) is retained, while the physics-informed component $\mathcal{L}_{\text{phys}}$ is omitted.

Fig. 12(a) shows the spatially and frequency-averaged relative L_2 error as a function of the SNR, while Fig. 12(b) presents the corresponding mean cosine similarity. In both figures, results obtained with the physics-informed DeepONet are shown in blue, whereas the purely data-driven model is depicted in orange.

The results clearly demonstrate that the physics-informed DeepONet achieves improved STI predictions, particularly in the high-noise (low-SNR) regime. At low SNR values, the physics-informed model consistently outperforms the purely data-driven network across both error metrics. This improvement can be attributed to the regularizing effect of the physics-based loss, which stabilizes the training process under noisy conditions and enforces physically consistent predictions. For cleaner signals (SNR > 30 dB), the difference in average error between the two approaches becomes negligible. In the low-noise regime, the purely data-driven model achieves comparable performance, indicating that when sufficient high-quality training data are available, the data alone provide enough information for the DeepONet to accurately learn the underlying operator.

To further investigate scenarios with limited training data, an additional parameter study has been conducted to examine the effect of the physics loss as a function of the training set size. The results of this study are shown in Fig. 13, where the relative L_2

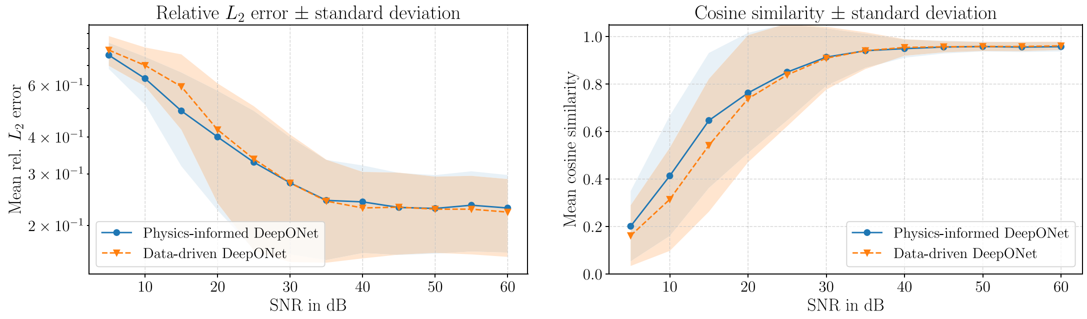

(a) Mean relative L_2 error over the SNR of the noise.

(b) Mean cosine similarity over the SNR of the noise.

Fig. 12. Comparison between the physics-informed DeepONet and the purely data-driven DeepONet. The left plot depicts the mean relative L_2 error of the STI predictions, while the right plot shows the mean cosine similarity, both as functions of the SNR of the training data. Shaded areas represent one standard deviation around the mean. Color legend: blue = physics-informed DeepONet, orange = data-driven DeepONet.

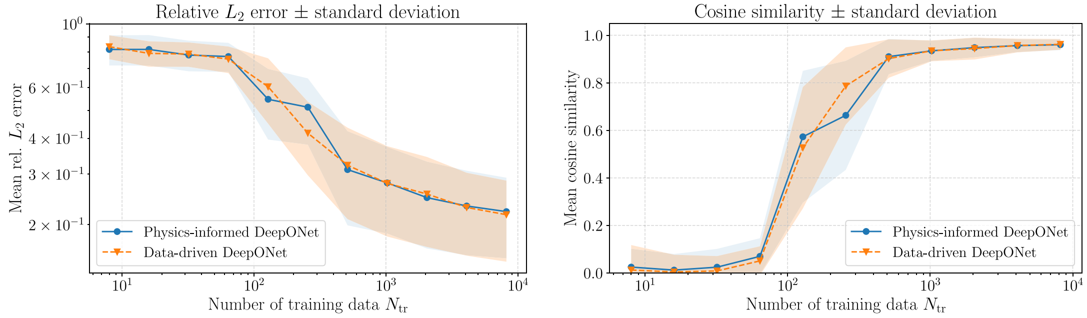

(a) Mean relative L_2 error over the number of training data $N_{\rm tr}$.

(b) Mean cosine similarity over the number of training data $N_{\rm tr}$.

Fig. 13. Comparison of the physics-informed and purely data-driven DeepONet models. The left plot shows the mean relative L_2 error of the STI predictions, while the right plot presents the mean cosine similarity, both plotted as functions of the number of training samples $N_{\rm tr}$. Shaded regions indicate one standard deviation around the mean. Color legend: blue = physics-informed DeepONet, orange = data-driven DeepONet.

error and cosine similarity are depicted as functions of the number of training samples $N_{\rm tr}$. For both error measures, the physics-informed and purely data-driven approaches yield very similar frequency-averaged results. Overall, no significant improvement due to the physics loss is observed in these averaged metrics. At $N_{\rm tr} = 256$ training samples, a noticeable deviation occurs, where the physics-informed DeepONet exhibits less reliable convergence and produces biased results. However, this behavior is interpreted as an outlier rather than a systematic trend. In the low-data regime (up to $N_{\rm tr} = 124$ training samples), the physics-informed DeepONet tends to show a slight performance advantage in terms of cosine similarity, however, this improvement remains marginal.

These findings are consistent with the previous observations and indicate that the incorporation of physics information provides only a slight benefit with respect to frequency-averaged prediction accuracy. Similar conclusions have been reported in prior studies on physics-informed neural networks, where the inclusion of physics-based loss terms led to only modest performance gains [81,95,96].

To obtain deeper insight beyond frequency-averaged metrics, the prediction errors of the STI field are additionally analyzed as functions of frequency. Fig. 14 presents the frequency-resolved cosine similarity for an exemplary case with $N_{\rm tr} = 512$ training samples. Although the physics-informed and purely data-driven DeepONet models exhibit comparable mean performance when averaged over frequency, the frequency-resolved analysis reveals that the physics-informed model consistently yields improved predictions at frequencies close to the system's eigenfrequencies. This behavior can be attributed to the stabilizing and regularizing effects of the physics-based loss term, which preserves physical consistency despite large amplitude variations at resonances.

Since practical structural dynamics applications are typically particularly concerned with the response near resonance frequencies, this slight performance advantage is highly relevant for practical applications. While the benefits of incorporating physics information become small or insignificant for large training sets and low-noise data, the physics-informed formulation provides a measurable improvement near eigenfrequencies and under high-noise conditions. These results therefore justify the inclusion of the physics-based loss in the present work, despite the associated increase in training complexity.

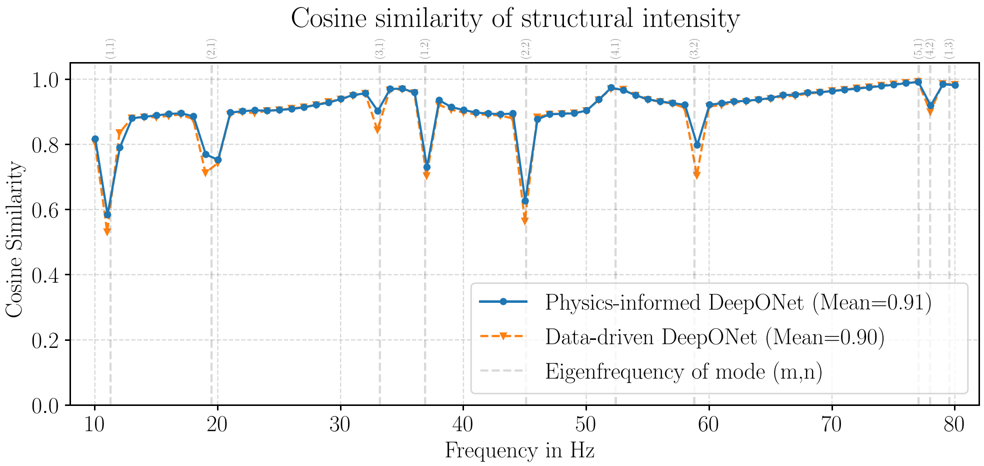

Fig. 14. Frequency-resolved error analysis of the STI predictions using the cosine similarity error metric at $N_{\mathrm{tr}} = 512$ training data samples. Color legend: blue = physics-informed DeepONet, orange = data-driven DeepONet, gray = analytical eigenfrequencies of the plate with corresponding mode numbers. All errors are evaluated with respect to the analytical reference solution.

5. Experimental validation

To validate the proposed DeepONet methodology using experimental data, LDV measurements have been performed on a thin plate by Zettel et al. [97] at the Institute of Aeroelasticity, German Aerospace Center (DLR). A detailed description of the experimental setup and a comprehensive analysis of the measurement results are provided in [97]. This work only summarizes the aspects relevant for understanding the measurement data within the context of DeepONet training.

5.1. Laser Doppler vibrometry measurement setup

The test specimen consists of a thin aluminum plate with a thickness of 1 mm and in-plane dimensions of 450 × 300 mm. It is embedded within a surrounding frame measuring 100 mm in width and 30 mm in thickness, resulting in an overall structure size of 650 × 400 mm. The plate and frame are milled from a single monolithic aluminum block to ensure homogeneous material properties and minimize residual stresses. Due to its high mass, the surrounding frame effectively imposes clamped boundary conditions on the plate.

The plate is excited by two electrodynamic shakers mounted perpendicular to the plate surface at positions $[x_{S1} = 437.5\,\mathrm{mm},\ y_{S1} = 175\,\mathrm{mm}]$ and $[x_{S2} = 212.5\,\mathrm{mm},\ y_{S2} = 325\,\mathrm{mm}]$, with the origin defined at the lower-left corner of the frame. The shakers are driven by pseudorandom noise signals, band-limited to 10 – 2000 Hz and sampled at 12.8 kHz. A phase shift of 180° is imposed between the two signals, such that the second shaker receives the inverted signal of the first shaker. This excitation scheme is designed to produce operating conditions in which the plate vibration response at the second shaker is approximately 90° out of phase with its driving force. Under this condition, the second shaker acts as a dynamic absorber, effectively functioning as a viscous damper and structural energy sink. In combination with the first shaker as the source, this two-shaker setup creates a active STI flow from source to sink. It should be noted that the second shaker is not integrated into an active control loop and thus cannot maintain the ideal phase shift of 90° over a broad frequency range. Instead, the ideal phase shift is only achieved at specific discrete frequencies. Impedance heads are installed at both shaker locations to simultaneously measure both excitation force and acceleration response, enabling verification of the intended phase condition. A detailed analysis of the phase relationship at the impedance head is provided in [97].

The transverse structural response of the plate is measured using LDV. The recorded time-domain signals are transformed into the frequency domain via discrete Fourier transform using a Hanning window and an overlap factor of 0.66. Each point is recorded over an acquisition time of 15 s at a sampling rate of 12.8 kHz.

5.2. Finite element method reference model

To verify the measurement data, a numerical reference model of the tested plate was created based on the FEM using the software COMSOL Multiphysics® [98]. The FEM model reproduces the geometry of the test specimen, consisting of a rectangular plate with dimensions of 450 × 300 mm and a thickness of 1 mm. In contrast to the experiment, the plate is modeled with clamped boundary conditions. For geometric comparability with the experimental configuration, the lower-left corner of the plate is positioned at $[x_O = 100\,\mathrm{mm}, y_O = 175\,\mathrm{mm}]$ to account for the surrounding frame.

The plate is discretized using shell elements that satisfy the Kirchhoff–Love plate equation, cf. Eq. (3), in the special case of a thin, flat plate. Aluminum is modeled as a linear-elastic, isotropic material with the properties $E = 67\,\mathrm{GPa}$, $\rho = 2700\,\mathrm{kg/m^3}$, and

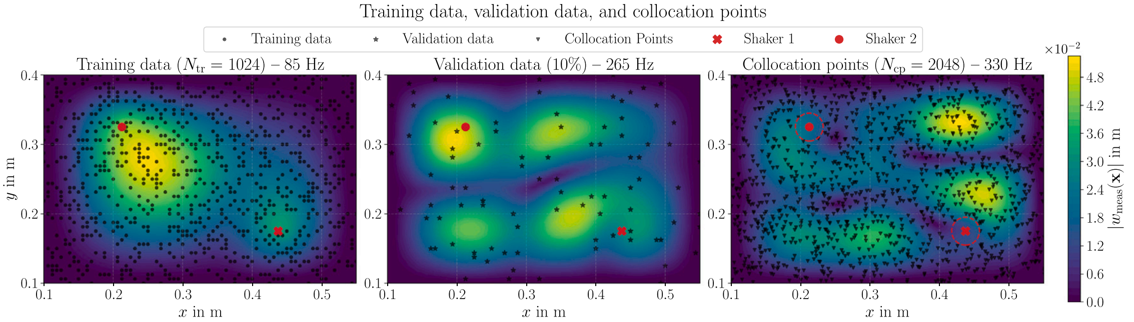

Fig. 15. Visualization of the data setup used for DeepONet training based on experimental data. Shown are the measured transverse displacement fields $w_{\text{meas}}(f)(\mathbf{x})$ at selected frequencies, along with the spatial distribution of training data points, validation points, and collocation points. The positions of the first shaker (source) and the second shaker (sink) are marked. Circular regions in the collocation point plot indicate areas excluded from residual evaluation to prevent sampling near singularities.

$\mu = 0.34$. Excitation is applied as a unit point force of 1 N in the out-of-plane z-direction at $[x_F = 437.5\,\text{mm},\ y_F = 175\,\text{mm}]$, while damping is introduced via an ideal viscous damper, oriented perpendicular to the plate surface, at $[x_D = 212.5\,\text{mm},\ y_D = 325\,\text{mm}]$ with a damping coefficient of $20\,\text{Ns/m}$. This purely vertical loading configuration induces pure flexural vibrations, allowing in-plane waves to be neglected. The Kirchhoff–Love plate equation is solved in the frequency domain over a frequency range of 50 – 400 Hz. The mesh is selected according to a wave number analysis to ensure a minimum of ten quadratic shell elements per wavelength [99]. After computation, both the transverse displacement field and the STI field from the FEM solution are exported and used as reference for subsequent analyses involving the measurement dataset.

Further details on the numerical model are provided in [97]. It should be noted that the FEM model reproduces the STI fields only qualitatively, as the excitation and damping parameters were not tuned to match the measured amplitudes. However, since the present study primarily focuses on the directional characteristics of the STI, this qualitative agreement is sufficient for the intended comparison.

In addition, it should be emphasized that, in contrast to the analytical ground truth solution presented in Section 4.2, the FEM reference model does not constitute an exact ground truth. Instead, it represents a numerical approximation of the true solution, whose accuracy depends critically on the correct specification of boundary conditions and unknown model parameters. In the present study, a highly controlled experimental plate example is chosen, cf. Section 5.1, where the boundary conditions are well characterized and the FEM model is carefully calibrated against the measurement data. Under these conditions, the resulting FEM solution can be regarded as a reasonable and reliable ground truth reference solution for validation purposes. Details of the model calibration procedure are provided in Ref. [97].

5.3. Measurement training data selection

Using the LDV measurement setup described in Section 5.1, the transverse displacement field is recorded at 3577 uniformly distributed measurement positions across the vibrating part of the plate, corresponding to a regular grid of 73 × 49 points along the x- and y-axes. From the originally acquired frequency range of 10 – 2000 Hz, only the interval from 50 – 400 Hz is considered in the present study, as it contains the first ten plate modes. For each frequency step of 5 Hz within this range, the dataset contains the spatial coordinates $[x, y]$ of all measurement points, together with the real and imaginary parts of the Fourier-transformed transverse displacement field.

Given the comparatively high cost and effort associated with acquiring experimental data, only $N_{\text{tr}} = 1024$ training samples are randomly selected per frequency. These samples are selected independently for each frequency using LHS to ensure space-filling coverage of the measurement domain and support robust generalization of the DeepONet. As detailed in Section 4.4, the selected data are split into a training set and a 10% validation set. All inputs are normalized to the range $[-1, 1]$ using min–max scaling parameters computed from the training set, which are stored for rescaling during inference. The collocation set, consisting of $N_{\text{cp}} = 2048$ points, is generated following the procedure in Section 4.4, with the only modification that the exclusion radius is reduced to 0.02 m to account for the smaller plate dimensions. It should be emphasized that no artificial noise is added to the experimental dataset, as the measurements inherently contain measurement noise.

Fig. 15 shows the spatial distribution of training data, validation data, and collocation points for the measurement dataset, analogous to Fig. 6. In this experimental case, the color map represents the magnitude of the measured displacement field $w_{\text{meas}}(f)(\mathbf{x})$. The frequencies shown correspond to operating conditions in which the phase difference between the force at second shaker and the plate response at the same location is approximately 90°, thereby acting similarly to a viscous damper, as discussed in Section 5.1.

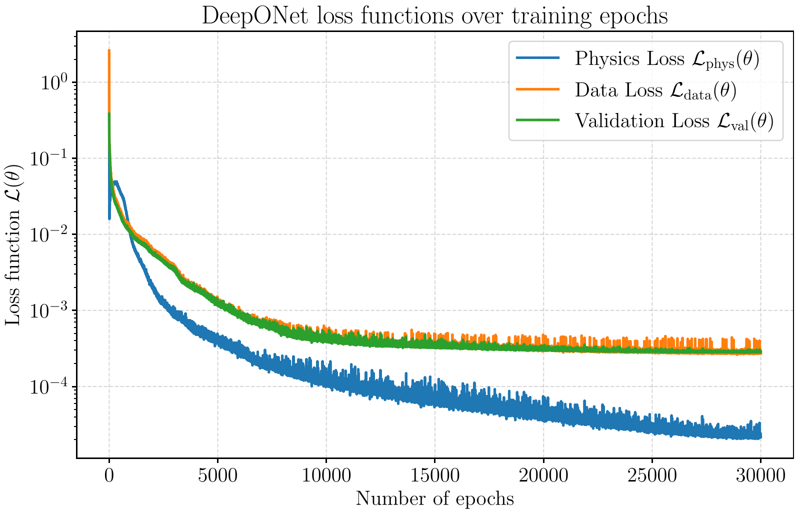

Fig. 16. Evolution of the loss functions during DeepONet training using measurement data, plotted as a function of the number of training epochs. The individual loss terms, physics loss $\mathcal{L}_{\text{phys}}$, data loss $\mathcal{L}_{\text{dat}}$, and validation loss $\mathcal{L}_{\text{val}}$, are displayed individually to illustrate their respective convergence behavior during training. Color legend: blue = physics loss $\mathcal{L}_{\text{phys}}$, orange = data loss $\mathcal{L}_{\text{data}}$, green = validation loss $\mathcal{L}_{\text{val}}$.

5.4. DeepONet training on measurement data

For the experimental validation of the proposed DeepONet methodology, a DeepONet is trained on the experimental training dataset described in Section 5.3. The network architecture and all training hyperparameters are kept identical to those used in the analytical investigations on the analytical plate model, as detailed in Section 3.4.

Fig. 16 shows the evolution of the individual loss components during training with experimental data. Similar to the analytical case, all loss terms exhibit clear and stable convergence behavior. The physics-informed loss $\mathcal{L}_{\text{phys}}$ shows a slight deviation during the initial training phase, likely caused by the relatively high initial learning rate or minor imbalances in the loss weighting. However, the optimization algorithm quickly compensates for this, and $\mathcal{L}_{\text{phys}}$ converges steadily over the course of training, eventually reaching MSE values in the order of 10^{-5}, even lower than the data-driven loss term.

In comparison to Fig. 6, it is evident that the asymptotic loss values obtained with measurement data are more than an order of magnitude higher than those in the analytical case. This finding indicates that learning a frequency-dependent operator directly from experimental data is inherently more challenging. This difficulty arises because measurements unavoidably exhibit higher measurement noise, sensor tolerances, and additional sources of uncertainty, which degrade signal quality and reduce the fidelity of the training data. Moreover, as explained in Section 5.1, the experimental phase mismatch from the ideal 90° phase condition of the two shakers introduces a frequency-dependent inconsistency in the data, which intrinsically complicates operator learning and leads to slower convergence and higher residual losses relative to the analytical case.

5.5. DeepONet structural intensity prediction

After training the physics-informed DeepONet on the measurement dataset, the displacement field w_θ and q_θ are first evaluated, followed by the computation of the STI field from the predictions. The procedure follows the same approach described in Secs 4.6 and 4.7, with the only difference that, for experimental data, the DeepONet is evaluated on the full set of measurement grid points during the inference stage. It should be emphasized that the full measurement grid (73 × 49) used for evaluating the numerical derivatives comprises a total of 3577 data points, which exceeds the number of samples used for DeepONet training ($N_{\text{tr}} = 1024$). Consequently, any deviations between the DeepONet predictions and the numerically differentiated results can be attributed solely to the generalization capability of the neural operator rather than differences in training data size. Evaluating both approaches on the same complete measurement grid enables a direct comparison of the predicted and measured displacement fields at exact measurement locations.

Since no analytical reference exists for the STI field in the experimental case, the numerical FEM model is used as the reference for STI error assessment. As discussed in Section 5.2, only the directional error can be quantified with respect to the FEM reference, while magnitude errors between the different STI prediction methods can be compared only qualitatively or relative to each other, since the numerical model is based on a generic unit excitation. Fig. 17 presents the STI prediction results based on the measurement data. Each subplot shows the normalized STI magnitude $|\mathbf{I}|$ alongside the corresponding STI vector field $[I_x, I_y]$, illustrating the direction of energy flow. The left column displays the FEM reference, the middle column the DeepONet predictions, and the right column the STI fields obtained via numerical differentiation of the measured transverse displacements after Savitzky–Golay filtering. The rows correspond to selected frequencies that satisfy the 90° phase shift discussed in Section 5, with the frequencies indicated

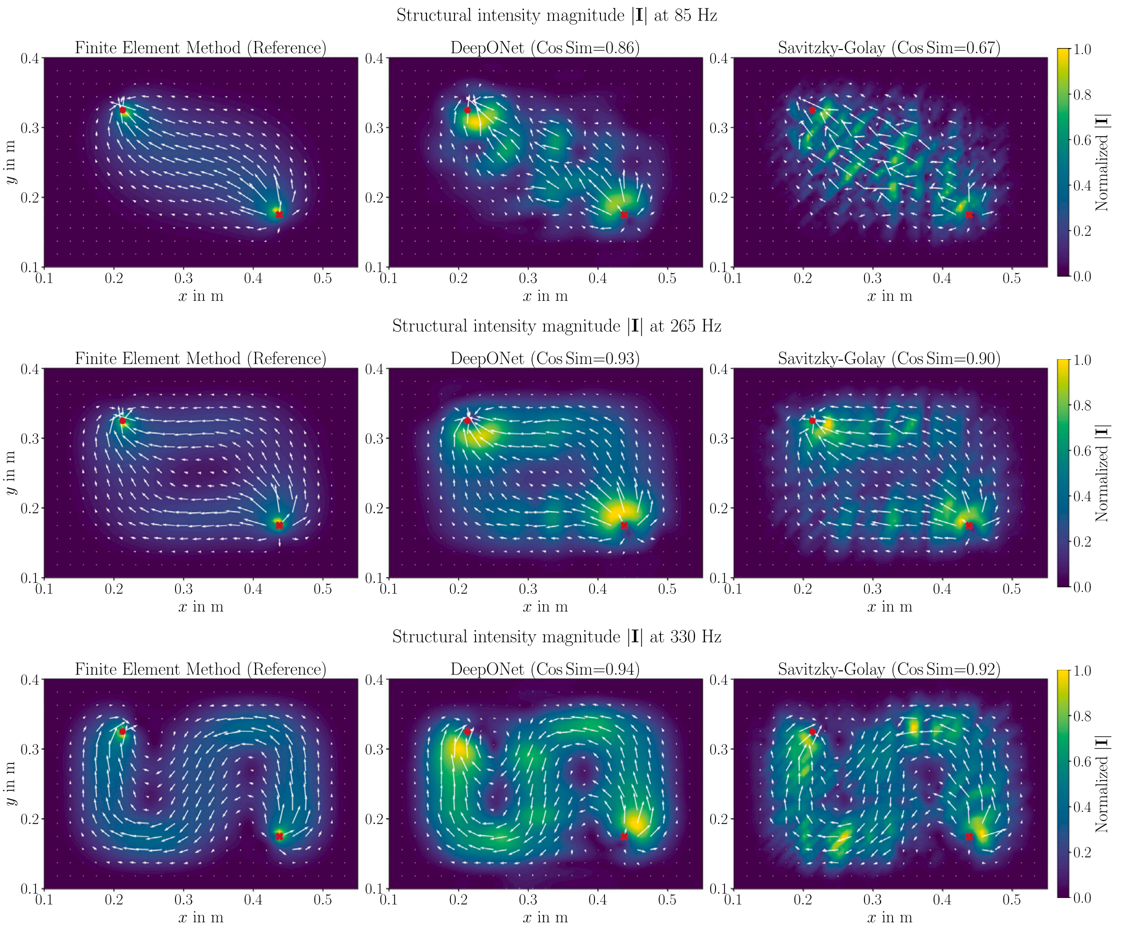

Fig. 17. Comparison of STI fields computed using the FEM (left column), the DeepONet prediction (middle column), and numerical differentiation using the Savitzky–Golay filter (right column). The results are presented for selected frequencies (organized by row), as specified in the subplot titles. The locations of the first shaker (source) and the second shaker (sink) are indicated by a red cross and a red point, respectively.

in the subplot titles. Quantitative assessment of prediction accuracy is provided in terms of the cosine similarity with respect to the FEM reference.

In general, Fig. 17 shows that both DeepONet and the numerically differentiated Savitzky–Golay approach capture the main directional structure of the FEM reference. However, DeepONet consistently achieves slightly higher cosine similarity values, particularly at lower frequencies (e.g., 85 Hz), where the improvement is most pronounced. In terms of amplitudes, the numerical differentiation approach exhibits localized artifacts and stripe-like patterns, similar to those observed in Fig. 8, while the DeepONet produces smoother and more coherent STI fields, indicating better robustness to measurement noise.

When comparing amplitude distributions between DeepONet and FEM, it should be noted that the FEM reference shows locally exaggerated STI magnitudes near the excitation and damping points due to the point-load and point-damper modeling. This effect reduces the relative prominence of the STI field in between after normalization compared to the DeepONet results. Slight amplitude overestimations near the shaker positions are also evident in the measurement-based predictions, likely caused by the spatially distributed nature of the shaker excitation rather than idealized discrete forces. Overall, the STI vector directions show strong agreement with the FEM reference, confirming the validity and applicability of the proposed DeepONet methodology also for experimental data.

Fig. 18 present the spatially averaged error metrics of the STI predictions based on experimental data as functions of frequency. Fig. 18(a) shows the relative L_2 error, while Fig. 18(b) depicts the cosine similarity. As in Fig. 9, the results for the different STI prediction methods are compared, and the relative L_2 error of the displacement field w_θ is additionally included. All error metrics are computed with respect to the numerical FEM reference solution.

The results show trends consistent with those observed in the analytical study. Across the entire frequency range, the DeepONet achieves the lowest amplitude and directional errors, while Savitzky–Golay–filtered numerical differentiation provides a clear improvement over unfiltered numerical differentiation. Interestingly, for experimental data, Savitzky–Golay–filtered numerical differentiation performs relatively better compared to the DeepONet than in the analytical case. This is attributed to the fact that, in

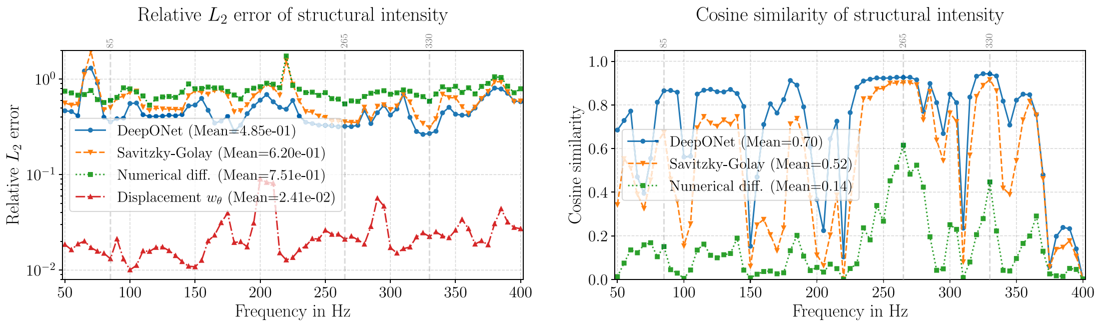

(a) Relative L_2 error as a function of frequency.

(b) Cosine similarity as a function of frequency.

Fig. 18. Error analysis of the STI predictions from the experimental data as a function of frequency. The left plot presents the relative L_2 error, while the right plot shows the cosine similarity. All results are evaluated with respect to the FEM-based reference solution. Color legend: blue = DeepONet prediction, orange = Savitzky–Golay filtered numerical differentiation, green = numerical differentiation without filtering, red = relative L_2 error of the DeepONet-predicted displacement field w_θ, gray = identified frequencies where the second shaker acts as a viscous damper.

measured plate vibrations, material damping reduces resonance-induced magnitude amplifications, thereby mitigating the exploding gradient issue that affected the numerical differentiation of the analytical dataset, see Fig. 8.

Overall, prediction accuracy is reduced when using experimental data compared to the analytical case. Specifically, the mean cosine similarity of the DeepONet predictions decreases from 0.95 in the analytical case to 0.70 with measurement data, and the mean relative L_2 error of the displacement field increases by nearly an order of magnitude from 4.4×10^{-3} to 2.41×10^{-2}.

This reduction can be partly attributed to inherent experimental factors, namely increased measurement noise, positioning inaccuracies, and deviations from ideal boundary conditions. More importantly, as discussed in Section 5.1, the dominant factor is the phase relationship in the dual-shaker setup. The ideal 90° phase shift between the exciting and damping shakers, required to emulate an ideal viscous damper, cannot be maintained uniformly across the 50 – 400 Hz range, in contrast to the FEM reference where this condition is enforced exactly. Consequently, frequency-averaging over the entire frequency range yields a lower cosine similarity that is primarily driven by experimental phase mismatch rather than limitations of the DeepONet methodology.

Consistent with this interpretation, Fig. 18(b) shows that, in frequency intervals where the experimental phase relation is close to the ideal 90°, the cosine similarity exceeds 0.9, whereas pronounced drops occur at frequencies where the phase requirement is not satisfied. Fig. 18(b) further confirms that the previously identified frequencies, indicated in gray, fall within these specific frequency bands. The verification of the 90° phase condition and the selection procedure for these frequencies are detailed in Ref. [97].

5.6. Parameter study on the number of measurement training data

After validating the applicability of the proposed DeepONet methodology on experimental data, a final parameter study is conducted to answer the question of how many spatial measurement data points are required per frequency to achieve an STI prediction of sufficient accuracy. In analogy to Section 4.8, which was based on the analytical solution, the number of training samples from the experimental dataset is systematically varied. As described in Section 5.3, the training data are selected from the full measurement dataset using random LHS sampling. In this study, the number of training points is increased stepwise from $N_{\mathrm{tr}} = 8 - 3577$ in powers of two, where 3577 training data points represent the full measurement dataset. All other network and training parameters are kept identical to those in Section 5.4. Fig. 19 presents the results of this parameter study. Fig. 19(a) shows the relative L_2 errors of the different STI predictions, averaged over all frequencies and spatial positions, together with the L_2 error of the predicted displacement field w_θ. The corresponding averaged cosine similarities are depicted in Fig. 19(b). All error measures are referenced to the numerical FEM solution, and the shaded areas represent one standard deviation around the mean.

The results follow the same trend as in the analytical case, indicating that prediction accuracy generally improves with increasing training data size, both in amplitude and directional error. Convergence is achieved at approximately $N_{\mathrm{tr}} = 1024$ training samples, beyond which additional data do not yield further improvements. In contrast to the analytical study in Section 4.8, the cosine similarity here slightly degrades beyond 1024 training samples, which can be attributed to randomness in the LHS and the higher variability inherent in the measurement data.

Unlike the analytical results in Fig. 10, the standard deviation of the DeepONet prediction error in the experimental case increases with larger datasets. This behavior can be attributed to the inherently high variance of STI predictions over the full frequency range when using measurement data, caused by the insufficient fulfillment of the assumed 90° phase relationship across wide frequency intervals, cf. Fig. 18. For very small training datasets ($N_{\mathrm{tr}} \leq 32$), the DeepONet output is essentially noise-like, leading to uniformly poor predictions with low overall variance. As the training dataset increases, the DeepONet captures the STI field characteristics more accurately, revealing the underlying frequency-dependent variability of the measurement data. This variance remains approximately constant once prediction quality saturates, confirming that it originates from limitations of the measurement data rather than the DeepONet approximation.

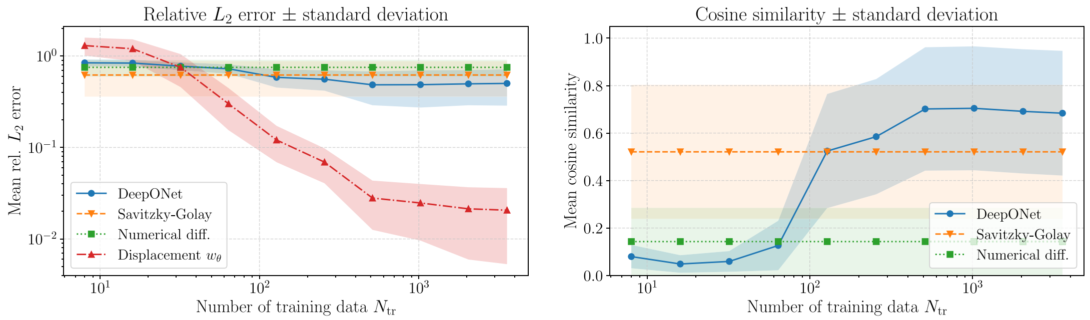

(a) Mean relative L_2 error as a function of the number of training data samples from experimental data.

(b) Cosine similarity as a function of the number of training data samples from experimental data.

Fig. 19. Results of the parameter study investigating the effect of training data quantity on the performance of the DeepONet model using experimental data. The left plot shows the mean relative L_2 error for the DeepONet prediction of the STI and the corresponding displacement field approximation, while the right plot displays the mean cosine similarity of the STI prediction, both as functions of the number of training data. Shaded regions indicate one standard deviation around the mean. Color legend: blue = DeepONet STI prediction, red = DeepONet displacement field approximation, orange = Savitzky–Golay filtered numerical differentiation, green = numerical differentiation without filtering. The numerical differentiation results are evaluated on the full measurement grid and are therefore independent of the number of training samples. All errors are computed with respect to the FEM-based reference solution.

Overall, the results demonstrate that the DeepONet methodology outperforms numerical differentiation in both amplitude accuracy and directional characteristics of the STI field, even when trained on a relatively small training data size of $N_{\mathrm{tr}} \geq 128$ samples.

6. Conclusions and outlook

This study has introduced a physics-informed deep operator network (DeepONet) framework for predicting structural intensity (STI) fields from noisy displacement data. In contrast to conventional numerical differentiation techniques, the proposed approach first learns a smooth, fully differentiable surrogate of the displacement field through neural network training. This surrogate enables stable and accurate computation of higher-order spatial derivatives via automatic differentiation, effectively mitigating the instabilities caused by differentiating noisy experimental data. As a result, the method facilitates robust and accurate STI estimation directly from measurements.

The methodology has been evaluated using two complementary case studies. First, an analytical benchmark problem of a simply supported plate has been employed to assess feasibility, perform detailed error analyses, and conduct parameter studies using the analytical reference solution. Second, the approach has been validated using experimental laser Doppler vibrometry (LDV) measurements of a plate structure. The results of both studies show that the physics-informed DeepONet accurately predicts both the transverse displacement field and the STI field across a broad frequency range, capturing both the magnitude distribution and the directional characteristics of the STI vectors with high accuracy. For the analytical benchmark, relative L_2 errors below 1×10^{-2} and cosine similarities of up to 0.99 are achieved, while for experimental data, cosine similarities above 0.9 are obtained despite inherent measurement uncertainties.

Across all studies, DeepONets consistently outperform numerical differentiation methods, both with and without Savitzky–Golay filtering, with the advantage being particularly pronounced at low frequencies, near plate resonances, and under high-noise (low-SNR) conditions. Parameter studies further indicate that increasing the amount of training data improves accuracy, although dataset sizes in the order of 10^3 measurement points are generally sufficient to achieve reliable predictions. These findings highlight the ability of physics-informed DeepONets to handle noisy measurement data and confirm the initial hypothesis that this data-driven, machine learning-based approach delivers high accuracy while being inherently more robust to noise than conventional numerical methods.

Despite its advantages, the DeepONet method also faces certain practical challenges. A key limitation is the requirement for a substantial number of high-quality labeled training data pairs, necessitating finely resolved displacement measurements. However, this limitation can be mitigated by the use of automated scanning LDV systems, which facilitate efficient acquisition of densely sampled measurement datasets. As with other machine learning approaches, the convergence behavior and final performance of the model are highly sensitive to the selection of network hyperparameters, often necessitating time-intensive tuning procedures. Nevertheless, the present study found the DeepONet training process to be remarkably stable and reliable across different configurations. For reference, training the DeepONet for 30,000 epochs with a constant batch size on a NVIDIA GeForce RTX 5080 GPU requires 6 h 5 min with 2048 training samples, whereas inference for a single forward pass only requires 0.039 s in average. Finally, the results presented in this paper are limited to academic plate models with well-defined boundary conditions and a carefully calibrated finite element model. Consequently, the direct transfer of the proposed approach to more complex real-world applications is only feasible to a limited extent, unless a reliable and well-established FEM reference model is available as ground truth.

As an outlook, future research will focus on extending the proposed methodology to more complex practical problems in structural dynamics. In particular, the estimation of STI from experimental data of real-world structures with uncertain boundary conditions and increased model uncertainty will be investigated. Such scenarios introduce the additional challenge of establishing a reliable ground truth reference solution for model validation. Potential application areas include STI analysis on curved surfaces and within three-dimensional solid structures, where numerous open research questions remain.

In summary, the presented physics-informed DeepONet methodology offers an accurate, noise-robust, and data-efficient framework for STI prediction from displacement measurements. This work demonstrates the potential of neural operators for data-driven STI analysis and opens new possibilities for machine learning-based approaches in experimental structural dynamics and noise control engineering.

Statements and declarations

- The contribution is part of the joint project *newAIDE* (19I21012F) under the consortium leadership of BMW AG with the partners Altair Engineering GmbH, divis intelligent solutions GmbH, MSC Software GmbH, and TWT GmbH. The project is supported by the Federal Ministry for Economic Affairs and Climate Action (BMWK) on the basis of a decision by the German Bundestag and the European Union.
- During the preparation of this work the authors used AI-assisted technologies for improving readability, language, and spelling only. After using these tools, the authors reviewed and edited the content as needed and take full responsibility for the content of the published article.

CRediT authorship contribution statement

Johannes D. Schmid: Writing – review & editing, Writing – original draft, Visualization, Validation, Supervision, Software, Project administration, Methodology, Investigation, Funding acquisition, Formal analysis, Data curation, Conceptualization. **Sebastian F. Zettel:** Writing – review & editing, Validation, Methodology, Investigation, Data curation. **Steffen Marburg:** Writing – review & editing, Supervision, Resources, Project administration, Funding acquisition.

Declaration of competing interest

The authors declare that they have no known competing financial interests or personal relationships that could have appeared to influence the work reported in this paper.

Acknowledgments

The authors would like to thank their colleagues from the numerical methods research group, in particular Jonas M. Schmid, Simone Preuss, and Mert Dogu for the valuable discussions.

Data availability

Data will be made available on request.

References

[1] G. Pavić, Measurement of structure borne wave intensity, part I: Formulation of the methods, J. Sound Vib. 49 (2) (1976) 221–230.
[2] M.V. van der Seijs, D. de Klerk, D.J. Rixen, General framework for transfer path analysis: History, theory and classification of techniques, Mech. Syst. Signal Process. 68–69 (2016) 217–244.
[3] D.U. Noiseux, Measurement of power flow in uniform beams and plates, J. Acoust. Soc. Am. 47 (1B) (1970) 238–247.
[4] J.W. Verheij, Cross spectral density methods for measuring structure borne power flow on beams and pipes, J. Sound Vib. 70 (1) (1980) 133–138.
[5] F.J. Fahy, R. Pierri, Application of cross-spectral density to a measurement of vibration power flow between connected plates, J. Acoust. Soc. Am. 62 (5) (1977) 1297–1298.
[6] E.G. Williams, H.D. Dardy, R.G. Fink, A technique for measurement of structure-borne intensity in plates, J. Acoust. Soc. Am. 78 (6) (1985) 2061–2068.
[7] R. Morikawa, S. Ueha, K. Nakamura, Error evaluation of the structural intensity measured with a scanning laser Doppler vibrometer and a k -space signal processing, J. Acoust. Soc. Am. 99 (5) (1996) 2913–2921.
[8] J.F. Arruda, Surface smoothing and partial spatial derivatives computation using a regressive discrete Fourier series, Mech. Syst. Signal Process. 6 (1) (1992) 41–50.
[9] J.-C. Pascal, J.-F. Li, X. Carniel, Wavenumber processing techniques to determine structural intensity and its divergence from optical measurements without leakage effects, Shock. Vib. 9 (1–2) (2002) 57–66.
[10] N.A. Halliwell, Laser-Doppler measurement of vibrating surfaces: A portable instrument, J. Sound Vib. 62 (2) (1979) 312–315.
[11] S.J. Rothberg, M.S. Allen, P. Castellini, D. Di Maio, J. Dirckx, D.J. Ewins, B.J. Halkon, P. Muyshondt, N. Paone, T. Ryan, H. Steger, E.P. Tomasini, S. Vanlanduit, J.F. Vignola, An international review of laser Doppler vibrometry: Making light work of vibration measurement, Opt. Lasers Eng. 99 (2017) 11–22.

[12] J. Arruda, P. Mas, Localizing energy sources and sinks in plates using power flow maps computed from laser vibrometer measurements, Shock. Vib. 5 (4) (1998) 235–253.
[13] J.D. Blotter, R.L. West, S.D. Sommerfeldt, Spatially continuous power flow using a scanning laser Doppler vibrometer, J. Vib. Acoust. 124 (4) (2002) 476–482.
[14] H. Weisbecker, B. Cazzolato, S. Wildy, S. Marburg, J. Codrington, A. Kotousov, Surface strain measurements using a 3D scanning laser vibrometer, Exp. Mech. 52 (7) (2012) 805–815.
[15] J.-C. Pascal, X. Carniel, J.-F. Li, Characterisation of a dissipative assembly using structural intensity measurements and energy conservation equation, Mech. Syst. Signal Process. 20 (6) (2006) 1300–1311.
[16] J.-C. Pascal, X. Carniel, V. Chalvidan, P. Smigielski, Determination of phase and magnitude of vibration for energy flow measurements in a plate using holographic interferometry, Opt. Lasers Eng. 25 (4–5) (1996) 343–360.
[17] K. Saijyou, S. Yoshikawa, Measurement of structural and acoustic intensities using near-field acoustical holography, Japan. J. Appl. Phys. 35 (5S) (1996) 3167.
[18] T. Eck, S.J. Walsh, Measurement of vibrational energy flow in a plate with high energy flow boundary crossing using electronic speckle pattern interferometry, Appl. Acoust. 73 (9) (2012) 936–951.
[19] F. Pires, P. Muyshondt, W. Keustermans, S. Vanlanduit, N.B. Roozen, J. Dirckx, Structural intensity analysis of flat plates based on digital stroboscopic holography measurements, J. Sound Vib. 428 (2018) 168–178.
[20] F. Pires, S. Avril, S. Vanlanduit, J. Dirckx, Structural intensity assessment on shells via a finite element approximation, J. Acoust. Soc. Am. 145 (1) (2019) 312.
[21] F.S. Egner, L. Sangiuliano, R.F. Boukadia, S. van Ophem, W. Desmet, E. Deckers, Polynomial filters for camera-based structural intensity analysis on curved plates, Mech. Syst. Signal Process. 193 (2023) 110245.
[22] E. Meteyer, O. Robin, N. Madinier, F. Gautier, A. Berry, Structural intensity in thin plates and beams under transient and stationary forces using time-resolved, full-field optical slope measurements, J. Sound Vib. 588 (2024) 118502.
[23] S.A. Hambric, Power flow and mechanical intensity calculations in structural finite element analysis, J. Vib. Acoust. 112 (4) (1990) 542–549.
[24] L. Gavrić, G. Pavić, A finite element method for computation of structural intensity by the normal mode approach, J. Sound Vib. 164 (1) (1993) 29–43.
[25] L. Gavric, U. Carlsson, L. Feng, Measurement of structural intensity using a normal mode approach, J. Sound Vib. 206 (1) (1997) 87–101.
[26] S.A. Hambric, R.P. Szwerc, Predictions of structural intensity fields using solid finite elements, Noise Control Eng. J. 47 (6) (1999) 209.
[27] S.A. Hambric, P.D. Taylor, Comparison of experimental and finite element structure-Borne flexural power measurements for a straight beam, J. Sound Vib. 170 (5) (1994) 595–605.
[28] M.S. Khun, H.P. Lee, S.P. Lim, Structural intensity in plates with multiple discrete and distributed spring–dashpot systems, J. Sound Vib. 276 (3–5) (2004) 627–648.
[29] D.-S. Cho, T.-M. Choi, J.-H. Kim, N. Vladimir, Structural intensity analysis of stepped thickness rectangular plates utilizing the finite element method, Thin-Walled Struct. 109 (2016) 1–12.
[30] F. Pires, S. Vanlanduit, J.J.J. Dirckx, Structural intensity analysis on irregular shells, J. Vib. Acoust. 141 (1) (2019).
[31] P.J. Capasso, G. Petrone, N. Kleinfeller, S. de Rosa, C. Adams, Modeling of fiber composite structures for the calculation of the structural intensity, Compos. Struct. 262 (2021) 113631.
[32] X. Xu, H. Lee, C. Lu, The structural intensities of composite plates with a hole, Compos. Struct. 65 (3–4) (2004) 493–498.
[33] G. Petrone, M. de Vendittis, S. de Rosa, F. Franco, Numerical and experimental investigations on structural intensity in plates, Compos. Struct. 140 (2016) 94–105.
[34] X.D. Xu, H.P. Lee, Y.Y. Wang, C. Lu, The energy flow analysis in stiffened plates of marine structures, Thin-Walled Struct. 42 (7) (2004) 979–994.
[35] C. Schaal, J. Ebert, J. Bös, T. Melz, Relation between structural intensity-based scalars and sound radiation using the example of plate-rib models, J. Vib. Acoust. 138 (4) (2016).
[36] M.R. Shepherd, S.C. Conlon, F. Semperlotti, S.A. Hambric, Structural intensity modeling and simulations for damage detection, J. Vib. Acoust. 134 (5) (2012).
[37] N. Kleinfeller, J. Bös, T. Melz, Measurement of the structural intensity of curved shell structures by means of 3D laser vibrometry, in: M. Ochmann, M. Vorländer, J. Fels (Eds.), Proceedings of the 23rd International Congress on Acoustics: Integrating 4th EAA Euroregio 2019 : 9-13 September 2019 in Aachen, Germany, Deutsche Gesellschaft für Akustik, Berlin, Germany, 2019.
[38] H. Al Ba'ba'a, M.A. Attarzadeh, M. Nouh, Experimental evaluation of structural intensity in two-dimensional plate-type locally resonant elastic metamaterials, J. Appl. Mech. 85 (4) (2018).
[39] Y. Wang, J. Du, L. Cheng, Power flow and structural intensity analyses of acoustic black hole beams, Mech. Syst. Signal Process. 131 (2019) 538–553.
[40] M. Su, J. Du, Y. Liu, Z. Dai, X. Liu, Vibration and power flow analysis of a uniform beam coupled with an ABH beam with arbitrary angles, Mech. Syst. Signal Process. 234 (2025) 112810.
[41] S. Cuomo, V.S. Di Cola, F. Giampaolo, G. Rozza, M. Raissi, F. Piccialli, Scientific machine learning through physics–Informed neural networks: Where we are and what's next, J. Sci. Comput. 92 (3) (2022) 88.
[42] S. Marburg, B. Nolte, Computational Acoustics of Noise Propagation in Fluids - Finite and Boundary Element Methods, Springer Berlin / Heidelberg, Berlin, Heidelberg, 2008.
[43] S. Lanthaler, S. Mishra, G.E. Karniadakis, Error estimates for DeepONets: a deep learning framework in infinite dimensions, Trans. Math. Appl. 6 (1) (2022).
[44] M. Raissi, P. Perdikaris, G.E. Karniadakis, Physics-informed neural networks: A deep learning framework for solving forward and inverse problems involving nonlinear partial differential equations, J. Comput. Phys. 378 (2019) 686–707.
[45] G.E. Karniadakis, I.G. Kevrekidis, L. Lu, P. Perdikaris, S. Wang, L. Yang, Physics-informed machine learning, Nat. Rev. Phys. 3 (6) (2021) 422–440.
[46] S. Cai, Z. Mao, Z. Wang, M. Yin, G.E. Karniadakis, Physics-informed neural networks (PINNs) for fluid mechanics: a review, Acta Mech. Sin. 37 (12) (2021) 1727–1738.
[47] J.D. Schmid, P. Bauerschmidt, C. Gurbuz, M. Eser, S. Marburg, Physics-informed neural networks for acoustic boundary admittance estimation, Mech. Syst. Signal Process. 215 (2024) 111405.
[48] J.D. Schmid, S. Preuss, L. Maicher, S. Marburg, Boundary integral neural networks for acoustic radiation prediction from noisy boundary data, J. Theor. Comput. Acoust. 33 (03) (2025).
[49] C. Rao, H. Sun, Y. Liu, Physics-informed deep learning for computational elastodynamics without labeled data, J. Eng. Mech. 147 (8) (2021) 04021043.
[50] E. Haghighat, M. Raissi, A. Moure, H. Gomez, R. Juanes, A physics-informed deep learning framework for inversion and surrogate modeling in solid mechanics, Comput. Methods Appl. Mech. Engrg. 379 (2021) 113741.
[51] H. Guo, X. Zhuang, T. Rabczuk, A deep collocation method for the bending analysis of Kirchhoff plate, Comput. Mater. Contin. 59 (2) (2019) 433–456.
[52] Y. Gu, C. Zhang, M.V. Golub, Physics-informed neural networks for analysis of 2D thin-walled structures, Eng. Anal. Bound. Elem. 145 (2022) 161–172.
[53] J.-H. Bastek, D.M. Kochmann, Physics-informed neural networks for shell structures, Eur. J. Mech. A Solids 97 (2023) 104849.
[54] H. Bolandi, G. Sreekumar, X. Li, N. Lajnef, V.N. Boddeti, Physics informed neural network for dynamic stress prediction, Appl. Intell. 53 (22) (2023) 26313–26328.
[55] R. Liang, W. Liu, Y. Fu, M. Ma, Physics-informed deep learning for structural dynamics under moving load, Int. J. Mech. Sci. 284 (2024) 109766.

[56] E. Zhang, M. Dao, G.E. Karniadakis, S. Suresh, Analyses of internal structures and defects in materials using physics-informed neural networks, Sci. Adv. 8 (7) (2022) eabk0644.
[57] W. Zhou, Y.F. Xu, Damage identification for plate structures using physics-informed neural networks, Mech. Syst. Signal Process. 209 (2024) 111111.
[58] K. Azizzadenesheli, N. Kovachki, Z. Li, M. Liu-Schiaffini, J. Kossaifi, A. Anandkumar, Neural operators for accelerating scientific simulations and design, Nat. Rev. Phys. 6 (5) (2024) 320–328.
[59] N. Kovachki, Z. Li, B. Liu, K. Azizzadenesheli, K. Bhattacharya, A. Stuart, A. Anandkumar, Neural operator: Learning maps between function spaces with applications to PDEs, J. Mach. Learn. Res. 24 (89) (2023) 1–97.
[60] N. Boullé, A. Townsend, A mathematical guide to operator learning, in: Numerical Analysis Meets Machine Learning, in: Handbook of Numerical Analysis, vol. 25, Elsevier, 2024, pp. 83–125.
[61] L. Lu, P. Jin, G. Pang, Z. Zhang, G.E. Karniadakis, Learning nonlinear operators via DeepONet based on the universal approximation theorem of operators, Nat. Mach. Intell. 3 (3) (2021) 218–229.
[62] Z. Li, N. Kovachki, K. Azizzadenesheli, B. Liu, K. Bhattacharya, A. Stuart, A. Anandkumar, Fourier neural operator for parametric partial differential equations, in: International Conference on Learning Representations, 2021.
[63] A. Anandkumar, K. Azizzadenesheli, K. Bhattacharya, N. Kovachki, Z. Li, B. Liu, A. Stuart, Neural operator: Graph kernel network for partial differential equations, in: ICLR 2020 Workshop on Integration of Deep Neural Models and Differential Equations, 2019.
[64] J. He, S. Koric, S. Kushwaha, J. Park, D. Abueidda, I. Jasiuk, Novel DeepONet architecture to predict stresses in elastoplastic structures with variable complex geometries and loads, Comput. Methods Appl. Mech. Engrg. 415 (2023) 116277.
[65] S. Koric, A. Viswantah, D.W. Abueidda, N.A. Sobh, K. Khan, Deep learning operator network for plastic deformation with variable loads and material properties, Eng. Comput. (2023).
[66] M.M. Rashid, T. Pittie, S. Chakraborty, N.M.A. Krishnan, Learning the stress-strain fields in digital composites using Fourier neural operator, IScience 25 (11) (2022) 105452.
[67] M. Zhou, H. Song, W. Ye, W. Wang, Z. Lai, Parameter estimation of structural dynamics with neural operators enabled surrogate modeling, Mech. Syst. Signal Process. 237 (2025) 112914.
[68] H. Jin, B. Zhang, Q. Cao, E. Zhang, A. Bora, S. Krishnaswamy, G.E. Karniadakis, H.D. Espinosa, Characterization and inverse design of stochastic mechanical metamaterials using neural operators, Adv. Mater. (Deerfield Beach Fla.) (2025) e2420063.
[69] J.E. Wagner, S. Burbulla, M. de Benito Delgado, J.D. Schmid, Neural operators as fast surrogate models for the transmission loss of parameterized sonic crystals, in: NeurIPS 2024 Workshop on Data-Driven and Differentiable Simulations, Surrogates, and Solvers, 2024.
[70] K. Shukla, V. Oommen, A. Peyvan, M. Penwarden, N. Plewacki, L. Bravo, A. Ghoshal, R.M. Kirby, G.E. Karniadakis, Deep neural operators as accurate surrogates for shape optimization, Eng. Appl. Artif. Intell. 129 (2024) 107615.
[71] S. Goswami, M. Yin, Y. Yu, G.E. Karniadakis, A physics-informed variational DeepONet for predicting crack path in quasi-brittle materials, Comput. Methods Appl. Mech. Engrg. 391 (2022) 114587.
[72] N. Borrel-Jensen, S. Goswami, A.P. Engsig-Karup, G.E. Karniadakis, C.-H. Jeong, Sound propagation in realistic interactive 3D scenes with parameterized sources using deep neural operators, Proc. Natl. Acad. Sci. 121 (2) (2024) e2312159120.
[73] C.Q. Wang, E.H. Ong, H. Qian, N.Q. Guo, On the application of B-spline approximation in structural intensity measurement, J. Sound Vib. 290 (1–2) (2006) 508–518.
[74] A. Savitzky, M.J.E. Golay, Smoothing and differentiation of data by simplified least squares procedures, Anal. Chem. 36 (8) (1964) 1627–1639.
[75] G. Pavić, Structural surface intensity: An alternative approach in vibration analysis and diagnosis, J. Sound Vib. 115 (3) (1987) 405–422.
[76] L. Cremer, Structure-Borne sound: Structural vibrations and sound radiation at audio frequencies, third ed., SpringerLink Bücher, Springer-Verlag Berlin Heidelberg, Berlin, Heidelberg, 2005.
[77] G. Pavić, Structure–Borne energy flow, in: M.J. Crocker (Ed.), Handbook of Noise and Vibration Control, Wiley, 2007, pp. 232–240.
[78] K. Hornik, M. Stinchcombe, H. White, Multilayer feedforward networks are universal approximators, Neural Netw. 2 (5) (1989) 359–366.
[79] T. Chen, H. Chen, Universal approximation to nonlinear operators by neural networks with arbitrary activation functions and its application to dynamical systems, IEEE Trans. Neural Netw. 6 (4) (1995) 911–917.
[80] L. Lu, X. Meng, S. Cai, Z. Mao, S. Goswami, Z. Zhang, G.E. Karniadakis, A comprehensive and fair comparison of two neural operators (with practical extensions) based on FAIR data, Comput. Methods Appl. Mech. Engrg. 393 (2022) 114778.
[81] S.G. Rosofsky, H. Al Majed, E.A. Huerta, Applications of physics informed neural operators, Mach. Learn.: Sci. Technol. 4 (2) (2023) 025022.
[82] D. Ray, O. Pinti, A.A. Oberai, Deep Learning and Computational Physics, Springer Nature Switzerland, Cham, 2024.
[83] S. Goswami, A. Bora, Y. Yu, G.E. Karniadakis, Physics-informed deep neural operator networks, in: T. Rabczuk, K.-J. Bathe (Eds.), Machine Learning in Modeling and Simulation, in: Computational Methods in Engineering & the Sciences, Springer International Publishing, Cham, 2023, pp. 219–254.
[84] S. Wang, H. Wang, P. Perdikaris, Learning the solution operator of parametric partial differential equations with physics-informed DeepONets, Sci. Adv. 7 (40) (2021) eabi8605.
[85] V. Sitzmann, J. Martel, A. Bergman, D. Lindell, G. Wetzstein, Implicit neural representations with periodic activation functions, in: H. Larochelle, M. Ranzato, R. Hadsell, M. Balcan, H. Lin (Eds.), in: Advances in Neural Information Processing Systems, vol. 33, Curran Associates, Inc, 2020, pp. 7462–7473.
[86] S. Wang, Y. Teng, P. Perdikaris, Understanding and mitigating gradient flow pathologies in physics-informed neural networks, SIAM J. Sci. Comput. 43 (5) (2021) A3055–A3081.
[87] Z. Xiang, W. Peng, X. Liu, W. Yao, Self-adaptive loss balanced physics-informed neural networks, Neurocomputing (2022).
[88] Z. Chen, V. Badrinarayanan, C.-Y. Lee, A. Rabinovich, GradNorm: Gradient normalization for adaptive loss balancing in deep multitask networks, in: J. Dy, A. Krause (Eds.), Proceedings of the 35th International Conference on Machine Learning, in: Proceedings of Machine Learning Research, vol. 80, PMLR, 2018, pp. 794–803.
[89] R. Bischof, M.A. Kraus, Multi-objective loss balancing for physics-informed deep learning, Comput. Methods Appl. Mech. Engrg. 439 (2025) 117914.
[90] I. Loshchilov, F. Hutter, Decoupled weight decay regularization, in: International Conference on Learning Representations, 2019.
[91] A. Paszke, S. Gross, F. Massa, A. Lerer, J. Bradbury, G. Chanan, T. Killeen, Z. Lin, N. Gimelshein, L. Antiga, A. Desmaison, A. Kopf, E. Yang, Z. DeVito, M. Raison, A. Tejani, S. Chilamkurthy, B. Steiner, L. Fang, J. Bai, S. Chintala, Pytorch: An imperative style, high-performance deep learning library, in: Advances in Neural Information Processing Systems 32, Curran Associates, Inc, 2019, pp. 8024–8035.
[92] S.J. Wildy, Accuracy of quasi-static bending strain measurement using scanning laser Doppler vibrometry (SLDV), Exp. Tech. 40 (6) (2016) 1461–1468.
[93] R. Wu, Y. Li, S. Zhang, Strain fields measurement using frequency domain Savitzky–Golay filters in digital image correlation, Meas. Sci. Technol. 34 (9) (2023) 095115.
[94] J.V. Araújo dos Santos, H. Lopes, Savitzky-Golay smoothing and differentiation filters for damage identification in plates, Procedia Struct. Integr. 54 (2024) 575–584.
[95] Z. Li, H. Zheng, N. Kovachki, D. Jin, H. Chen, B. Liu, K. Azizzadenesheli, A. Anandkumar, Physics-informed neural operator for learning partial differential equations, ACM / IMS J. Data Sci. 1 (3) (2024) 1–27.
[96] X. Karakonstantis, D. Caviedes-Nozal, A. Richard, E. Fernandez-Grande, Room impulse response reconstruction with physics-informed deep learning, J. Acoust. Soc. Am. 155 (2) (2024) 1048–1059.
[97] S.F. Zettel, R. Winter, M. Böswald, M. Maeder, S. Marburg, Approximation of structural intensity from experimental structural response data using a hybrid method - methodology, verification and validation, 2025, http://dx.doi.org/10.2139/ssrn.5823455, Available at SSRN: https://ssrn.com/abstract=5823455.
[98] COMSOL multiphysics®, 2025, URL www.comsol.com. V6.3, COMSOL AB, Stockholm, Sweden.
[99] P. Langer, M. Maeder, C. Guist, M. Krause, S. Marburg, More than six elements per wavelength: The practical use of structural finite element models and their accuracy in comparison with experimental results, J. Comput. Acoust. 25 (04) (2017) 1750025.